Advances in Water Resources 173 (2023) 104390

Contents lists available at ScienceDirect

Advances in Water Resources

journal homepage: www.elsevier.com/locate/advwatres

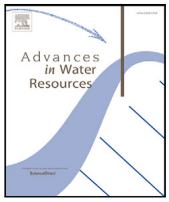

A hybridizable discontinuous Galerkin method on unfitted meshes for single-phase Darcy flow in fractured porous media ☆

Guosheng Fu [a], Yang Yang [b,*]

[a] Department of Applied and Computational Mathematics and Statistics, University of Notre Dame, USA
[b] Department of Mathematical Sciences, Michigan Technological University, USA

ARTICLE INFO

MSC:
65N30
65N12
76S05
76D07

Keywords:
Hybridizable discontinuous Galerkin method
Fractured porous media
Unfitted mesh
Dirac-δ function approach

ABSTRACT

We present a novel hybridizable discontinuous Galerkin (HDG) method on unfitted meshes for single-phase Darcy flow in a fractured porous medium. In particular we apply the HDG methodology to the recently introduced reinterpreted discrete fracture model (RDFM) that use Dirac-δ functions to model both conductive and blocking fractures. Due to the use of Dirac-δ function approach for the fractures, our numerical scheme naturally allows for unfitted meshes with respect to the fractures, which is the major novelty of the proposed scheme. Moreover, the scheme is locally mass conservative. In particular, our scheme has a simple form, which is a novel modification of an existing regular Darcy flow HDG solver by adding the following two components: (i) locate the co-dimension one fractures in the background mesh and add the appropriate surface integrals associated with these fractures into the stiffness matrix, (ii) adjust the penalty parameters on cells cut through conductive and blocking fractures (fractured cells).

Despite the simplicity of the proposed scheme, it performs quite well for various benchmark test cases in both two and three dimensions. *To the best of our knowledge,* this is the first time that an unfitted finite element scheme been applied to complex fractured porous media flow problems in 3D with both blocking and conductive fractures without any restrictions on the meshes.

1. Introduction

Many applications in contaminant transportation, petroleum engineering and radioactive waste deposit can be modeled by single- and multi-phase flows in porous media. A typical porous medium may contain conductive fractures with tiny thickness but high permeability. Some fractures may be filled with minerals and debris, forming blocking fractures with low permeability. Mathematical modeling and numerical simulation for flows in fractured porous media are challenging due to the high heterogeneity of the porous medium.

Several effective mathematical models have been developed in the literature for simulating flows in porous media with conductive fractures, such as the dual porosity model (Barenblatt et al., 1960; Warren and Root, 1963; Geiger et al., 2013), single porosity model (Ghorayeb and Firoozabadi, 2000), traditional discrete fracture model (DFM) (Noorishad and Mehran, 1982; Baca et al., 1984; Kim and Deo, 1999, 2000; Karimi-Fard and Firoozabadi, 2001; Geiger-Boschung et al., 2009; Zhang et al., 2013), embedded DFM (EDFM) (Li and Lee, 2008; Moinfar, 2013; Yan et al., 2016; Tene et al., 2017; Jiang and Younis, 2017; HosseiniMehr et al., 2018; Xu et al., 2019), the interface models (Alboin et al., 1999, 2000; Hansbo and Hansbo, 2002; Odsæter et al., 2019) and extended finite element DFM (XDFM) based on the interface models (Fumagalli and Scotti, 2014; Huang et al., 2011; Schwenck, 2015; Salimzadeh and Khalili, 2015; Flemisch et al., 2016), finite element method based on Lagrange multipliers (Köppel et al., 2019a,b; Schädle et al., 2019), etc. Among the above mentioned works, the interface model (Martin et al., 2005; Angot et al., 2009; Boon et al., 2018; Kadeethum et al., 2020), the projection-based EDFM (pEDFM) (Tene et al., 2017; Jiang and Younis, 2017), and XDFM (Flemisch et al., 2016) can also be used for problems containing blocking fractures. The interface model is to explicitly represent the fracture as the interface of the porous media, and the governing equations in the porous media and fractures can be constructed. In the interface model, the matrix and fractures are considered as two different systems and the mass transfer between them is given by the jump of the velocity. Therefore, the interface model requires a conforming mesh (fitted mesh), i.e. the fracture is located at the cell skeletons. Though

☆ G. Fu was partially supported by the NSF, United States grant DMS-2012031. Y. Yang was supported by the Simon Foundation, United States 961585.
* Corresponding author.
E-mail addresses: gfu@nd.edu (G. Fu), yyang7@mtu.edu (Y. Yang).

https://doi.org/10.1016/j.advwatres.2023.104390
Received 10 September 2022; Received in revised form 7 December 2022; Accepted 28 January 2023
Available online 8 February 2023

hanging nodes are allowed, numerical methods based on fitted meshes may suffer from low quality meshes. To fix this gap, XDFM (Fumagalli and Scotti, 2014; Huang et al., 2011; Schwenck, 2015; Salimzadeh and Khalili, 2015; Flemisch et al., 2016) was introduced. However, such treatment may significantly complicate the implementation in a general geometric setting, which is not of practical use, especially for problems with high geometrical complexity (Flemisch et al., 2018). Another possibility to extend the interface model to unfitted mesh is to use the CutFEM (Burman et al., 2019). However, this method may not work for media with complicated fractures, as the fractures have to separate the domain into completely disjoint subdomains. The pEDFM (Tene et al., 2017; Jiang and Younis, 2017) is another way to simulate flow in porous media with blocking fractures. The basic idea is to reduce the effective flow area between the blocking fracture and the adjacent matrix cells based on the property of the blocking fracture. However, most of previous work in this direction are based on structured box grids, and the extension to general simplicial meshes seems to be complicated; see a recent interesting work on pEDFM using hexahedral corner-point grid (CPG) geometries (HosseiniMehr et al., 2022).

In Xu and Yang (2020), one of the authors introduced the reinterpreted discrete fracture model (RDFM) for single-phase flow in porous media with conductive fractures. Different from the interface model and pEDFM, the RDFM couples the fracture and matrix in one system and use one equation to model the flows in both matrix and fractures. The basic idea is to use Dirac-δ functions to represent the lower dimensional fractures in the system containing higher dimensional matrix. The effect of the Dirac-δ functions is to increase the permeability at the location of the conductive fractures. Later, the RDFM was successfully applied to simulate contaminant transportation in Feng et al. (2021). As an extension, the RDFM was further developed to simulate flows in porous media with both conductive and blocking fractures in Xu et al. (2023). Similar to the RDFM for conductive fractures (Xu and Yang, 2020), the blocking fractures were also described as Dirac-δ functions, and they are used to increase the flow resistance. The RDFM incorporates information of the fractures into the equation, hence it works for arbitrary meshes without any restrictions. In Xu et al. (2023), the local discontinuous Galerkin (LDG) methods were applied to RDFM. An extremely large penalty of order $\mathcal{O}(h^{-3})$ was added to the pressure on cell interfaces without blocking fractures, while a moderate large penalty of order $\mathcal{O}(h^{-2})$ was applied to the normal direction of the velocity on cell interfaces with blocking fractures. The penalty is used to intimate the continuity requirement of the target variables. Unfortunately, this LDG method leads to a fully coupled saddle-point linear system for the velocity and pressure, hence its practical application in three dimensions is limited. Moreover, the lowest order scheme therein uses (discontinuous) piecewise linear functions as the piecewise constant version did not lead to a convergent algorithm. Furthermore, the effect of the penalty and well-posedness of the method was not clear. Besides the above work, the RDFM for blocking fractures was also combined with the interface model for conductive fractures in Fu and Yang (2022) where a fitted mesh for conductive fractures was required.

In this paper, we apply the hybridizable discontinuous Galerkin (HDG) methods for RDFM-based single-phase flows in porous media. Similar to the idea given in Xu et al. (2023), the proposed method (1) produces locally conservative velocity approximations; (2) works for problems containing both conductive and blocking fractures; (3) can be applied to arbitrary meshes without any restrictions. In additional to the above, there are several advantages of the proposed method that were not enjoyed by the one given in Xu et al. (2023). First of all, the HDG method can be efficiently solved via static condensation, which leads to a symmetric positive definite (SPD) linear system for the pressure degrees of freedom (DOFs) on the mesh skeletons only. Hence they can be implemented very efficiently comparing with the LDG scheme (Xu et al., 2023). As a result, three-dimensional simulations for complex fracture networks are now possible. Secondly, the penalty parameters in the HDG scheme are only adjusted on cells containing fractures, with extra (pressure) stabilization on conductive fractures and reduced (pressure) stabilization on blocking fractures. With a judicious choice of the penalty parameters, the lowest order HDG scheme with piecewise constant approximations can now yield satisfactory numerical results. Finally, the well-posedness of the proposed method can be guaranteed theoretically, which was completely missing for the method given in Xu et al. (2023). As an application, it is straightforward to couple the proposed flow equation with the transport equations and construct locally conservative numerical methods for the transport equations. However, that is not the main target of this paper, so we will discuss the applications in the future. The combination of these properties for the HDG scheme on unfitted meshes makes it highly competitive comparing with existing works for fractured porous media that can simultaneously handle blocking and conductive fractures both in terms of algorithmic complexity and numerical accuracy.

The rest of the paper is organized as follows. In Section 2, we present the RDFM and the HDG methods to be used. Numerical results for various benchmark test cases are presented in Section 3. Some concluding remarks will be given in Section 4.

2. The HDG scheme

In this section, we first introduce the RDFM (1) for fractured porous media flow. Then we convert it into an equivalent three-field formulation (2) that will be used for the HDG discretization. Next, we present details of the unfitted mesh HDG scheme (5) and establish its well-posedness. Moreover, we also comment on the (unfitted) mesh requirements, the choice of HDG stabilization parameters, its relation with regular porous media flow HDG solver, the extension to use alternative finite element spaces, efficient implementation via static condensation, and local mesh refinements near fractures. The performance of the scheme (5) will be validated via ample numerical studies in Section 3.

2.1. The model

We consider the following RDFM proposed in Xu et al. (2023):

$$\left(\boldsymbol{I}+\boldsymbol{K}_m\sum_{i=1}^{M}\frac{\epsilon_i}{k_i}\delta_{\Gamma_i}\boldsymbol{n}_i\boldsymbol{n}_i^T\right)\boldsymbol{u}=-\left(\boldsymbol{K}_m+\sum_{i=M+1}^{M+N}\epsilon_i k_i\delta_{\Gamma_i}(\boldsymbol{I}-\boldsymbol{n}_i\boldsymbol{n}_i^T)\right)\nabla p, \tag{1a}$$

$$\nabla\cdot\boldsymbol{u}=f, \tag{1b}$$

on a d-dimensional domain Ω with $d = 2,3$. Here $\boldsymbol{u}$ is the total Darcy velocity, p the pressure, $\boldsymbol{K}_m$ is the matrix permeability, $\boldsymbol{I}$ is the identity tensor, f is the source term, and Γ_i is the location of the ith $(d-1)$-dimensional fracture with thickness ϵ_i, permeability k_i and normal direction $\boldsymbol{n}_i$ for $1 \le i \le M+N$, where we assume the first M fractures are blocking fractures while the last N fractures are conductive fractures, i.e., $k_i \ll \boldsymbol{K}_m$ for $i \le M$ and $k_i \gg \boldsymbol{K}_m$ for $i \ge M+1$. Moreover, δ_{Γ_i} is the Dirac-δ function such that $\delta_{\Gamma_i}(\boldsymbol{x}) = \infty$ if $\boldsymbol{x} \in \Gamma_i$, $\delta_{\Gamma_i}(\boldsymbol{x}) = 0$ if $\boldsymbol{x} \notin \Gamma_i$ and $\int_\Omega \delta_{\Gamma_i}\mathrm{d}x = 1$. For simplicity, we assume the model (1) is equipped with the homogeneous Dirichlet boundary condition $p = 0$ on $\partial\Omega$. Other boundary conditions will be used in the numerical experiments.

Remark 2.1 (*On RDFM*)**.** In (1), we apply Dirac-δ functions to bridge the difference of the dimensions between the matrix and fractures. The first M Dirac-δ functions are used to increase the flow resistance and are for blocking fractures. Due to the small thickness of the blocking fractures, their effect in the tangential direction is negligible. Therefore, we only include the permeability tensor associated with the normal direction in the model. Similarly, the last N Dirac-δ functions are used to increase the permeability and are for conductive fractures. Moreover the effect of the conductive fractures in the normal direction

is negligible, and we only include the permeability tensor associated with the tangential direction in the model. We refer to Xu and Yang (2020) and Xu et al. (2023) for more discussion on the RDFM.

The Dirac-δ function approach in the above model avoids a direct modeling of the fractures using lower dimensional Darcy flows as typical in the interface models (Martin et al., 2005; Angot et al., 2009; Boon et al., 2018; Kadeethum et al., 2020). Hence, unfitted mesh discretizations can be naturally applied. In the original work (Xu et al., 2023), an LDG scheme on unfitted meshes was devised for (1) in two dimensions with satisfactory numerical results. However, well-posedness of the LDG scheme was not established as no energy identity exists, and its computational cost is relatively large comparing with existing works on (partially) fitted meshes.

Here we will devise a well-posed HDG scheme on unfitted meshes for the above model (1), which is not only computationally cheaper than the LDG scheme (Xu et al., 2023) but also more accurate and has an energy identity. To this end, we introduce the Darcy velocity in the matrix $\widetilde{\boldsymbol{u}} := -\boldsymbol{K}_m \nabla p$ as a new unknown and rewrite the model (1) into the following three-field formulation:

$$\left(\boldsymbol{K}_m^{-1} + \sum_{i=1}^{M} \frac{\epsilon_i}{k_i} \delta_{\Gamma_i} \boldsymbol{n}_i \boldsymbol{n}_i^T\right) \boldsymbol{u} = \left(\boldsymbol{I} + \sum_{i=M+1}^{M+N} \boldsymbol{K}_m^{-1} \epsilon_i k_i \delta_{\Gamma_i} (\boldsymbol{I} - \boldsymbol{n}_i \boldsymbol{n}_i^T)\right) \boldsymbol{K}_m^{-1} \widetilde{\boldsymbol{u}}, \tag{2a}$$

$$\boldsymbol{K}_m^{-1} \widetilde{\boldsymbol{u}} + \nabla p = 0, \tag{2b}$$

$$\nabla \cdot \boldsymbol{u} = f, \tag{2c}$$

Note that we multiplied Eq. (1a) with $\boldsymbol{K}_m^{-1}$ on the left to obtain Eq. (2a). We emphasize that here $\boldsymbol{u}$ is the total Darcy velocity that contains information about the fractures, whilst $\widetilde{\boldsymbol{u}}$ is the Darcy velocity on the matrix without fracture contributions.

2.2. The HDG scheme

Let $\mathcal{T}_h := \{K\}$ be a triangulation of the domain Ω that is unfitted to the location of the fractures. Let $\mathcal{E}_h$ be the collections of $(d-1)$-dimensional facets (edges for $d=2$, faces for $d=3$) of $\mathcal{T}_h$. We use level set functions to represent the fractures Γ_i. In particular,

- if Γ_i is a closed curve/surface without boundaries, it is simply approximated by the zero level set of a continuous piecewise linear function $\phi_i \in W_h^1 \cap H^1(\Omega)$ on the mesh $\mathcal{T}_h$:

  $$\Gamma_{i,h} := \{x \in \Omega : \phi_i(x) = 0\}.$$

- if Γ_i is a curve/surface with $(d-2)$-dimensional boundary $\partial\Gamma_i$, it is approximated by a main level set function $\phi_i \in W_h^1 \cap H^1(\Omega)$ for the (extended) surface Γ_i and additional level set functions $\psi_i^j \in W_h^1 \cap H^1(\Omega)$ for $j = 1, \dots, L$ to take care of the boundary $\partial\Gamma_i$:

  $$\Gamma_{i,h} := \{x \in \Omega : \phi_i(x) = 0\} \cap_{j=1}^{L} \{x \in \Omega : \psi_i^j(x) < 0\}.$$

  In practice, usually two level set functions are sufficient to provide a good approximation of Γ_i, i.e.,

  $$\Gamma_{i,h} := \{x \in \Omega : \phi_i(x) = 0\} \cap \{x \in \Omega : \psi_i^1(x) < 0\}.$$

Hence the discrete fractures $\Gamma_{i,h}$ on each element $K \in \mathcal{T}_h$ is always a line segment in 2D or a polygon in 3D due to the use of piecewise linear functions as level sets. With $\Gamma_{i,h}$ ready, we split the cells in $\mathcal{T}_h$ into three non-overlapping groups

$$\mathcal{T}_h := \mathcal{T}_h^r \cup \mathcal{T}_h^b \cup \mathcal{T}_h^c, \tag{3}$$

where $\mathcal{T}_h^r$ contains regular cells without fractures, $\mathcal{T}_h^b$ contains cells with blocking fractures, and $\mathcal{T}_h^c$ contains cells with conductive fractures defined as follows:

$$\begin{aligned}
\mathcal{T}_h^b &:= \{K \in \mathcal{T}_h : \quad \exists i \in [1, M] \text{ such that } K \cap \Gamma_{i,h} \neq \emptyset\},\\
\mathcal{T}_h^c &:= \{K \in \mathcal{T}_h \backslash \mathcal{T}_h^b : \exists i \in [M+1, M+N] \text{ such that } K \cap \Gamma_{i,h} \neq \emptyset\},\\
\mathcal{T}_h^r &:= \mathcal{T}_h \backslash \{\mathcal{T}_h^b \cup \mathcal{T}_h^c\}.
\end{aligned}$$

Remark 2.2 (*On Cell Splitting*). Here we require the splitting of the computational cells in (3) to be non-overlapping. This means that a blocking fractured cell in $\mathcal{T}_h^b$ cannot include conductive fractures, nor a conductive fractured cell in $\mathcal{T}_h^c$ can include blocking fractures. Such requirement is necessary for the well-posedness of the HDG scheme (5) defined below; see Theorem 2.1. Note that when both blocking and conductive fractures appear in a cell, we need to either ignore the blocking fractures or the conductive fractures in that cell. The latter is used in our numerical implementation. However, if the cell is dominated by the conductive fractures, we shall instead ignore the blocking fractures therein. Furthermore, our preliminary numerical results for Example 2 below (not reported here) suggest that it is not beneficial to include both conductive and blocking fractures on such cells in the formulation (5), which would produce large pressure oscillations near these cells. A more detailed study on the treatment of such mixed cells will be carried out in our future work.

Note that we allow fractures to be intersecting with each other in an arbitrary fashion within a single cell as long as a discrete characterization of the fracture $\Gamma_{i,h}$ using (multi-)level set functions is possible.

Given a polynomial degree $k \geq 0$, we consider the following finite element spaces:

$$\boldsymbol{V}_h^k := \{\boldsymbol{v} \in [L^2(\mathcal{T}_h)]^d : \ \boldsymbol{v}|_K \in [P_k(K)]^d, \quad \forall K \in \mathcal{T}_h\}, \tag{4a}$$

$$W_h^k := \{w \in L^2(\mathcal{T}_h) : \ w|_K \in P_k(K), \quad \forall K \in \mathcal{T}_h\}, \tag{4b}$$

$$M_h^k := \{\mu \in L^2(\mathcal{E}_h) : \ \mu|_F \in P_k(F), \quad \forall F \in \mathcal{E}_h, \quad \mu|_F = 0 \text{ on } \partial\Omega\}, \tag{4c}$$

where $P_k(S)$ is the polynomial space of degree at most k on S. We further denote the following inner products to simplify notation:

$$(\phi, \psi)_{\mathcal{T}_h} := \sum_{K \in \mathcal{T}_h} \int_K \phi\, \psi \, \mathrm{dx}, \qquad \langle \phi, \psi \rangle_{\partial \mathcal{T}_h} := \sum_{K \in \mathcal{T}_h} \int_{\partial K} \phi\, \psi \, \mathrm{ds}.$$

The HDG scheme for (2) is now given as follows: Find $(\boldsymbol{u}_h, \widetilde{\boldsymbol{u}}_h, p_h, \widehat{p}_h) \in \boldsymbol{V}_h^k \times \boldsymbol{V}_h^k \times W_h^k \times M_h^k$ such that

$$(\boldsymbol{K}_m^{-1} \boldsymbol{u}_h, \widetilde{\boldsymbol{v}}_h)_{\mathcal{T}_h} + \boldsymbol{\Phi}_b(\boldsymbol{u}_h, \widetilde{\boldsymbol{v}}_h) = (\boldsymbol{K}_m^{-1} \widetilde{\boldsymbol{u}}_h, \widetilde{\boldsymbol{v}}_h)_{\mathcal{T}_h} + \boldsymbol{\Phi}_c(\widetilde{\boldsymbol{u}}_h, \widetilde{\boldsymbol{v}}_h), \tag{5a}$$

$$(\boldsymbol{K}_m^{-1} \widetilde{\boldsymbol{u}}_h, \boldsymbol{v}_h)_{\mathcal{T}_h} - (p_h, \nabla \cdot \boldsymbol{v}_h)_{\mathcal{T}_h} + \langle \widehat{p}_h, \boldsymbol{v}_h \cdot \boldsymbol{n} \rangle_{\partial \mathcal{T}_h} = 0, \tag{5b}$$

$$-(\boldsymbol{u}_h, \nabla q_h)_{\mathcal{T}_h} + \langle \widehat{\boldsymbol{u}}_h \cdot \boldsymbol{n}, q_h \rangle_{\partial \mathcal{T}_h} = (f, q_h)_{\mathcal{T}_h}, \tag{5c}$$

$$\langle \widehat{\boldsymbol{u}}_h \cdot \boldsymbol{n}, \widehat{q}_h \rangle_{\partial \mathcal{T}_h} = 0, \tag{5d}$$

for all $(\boldsymbol{v}_h, \widetilde{\boldsymbol{v}}_h, q_h, \widehat{q}_h) \in \boldsymbol{V}_h^k \times \boldsymbol{V}_h^k \times W_h^k \times M_h^k$, where $\boldsymbol{\Phi}_b/\boldsymbol{\Phi}_c$ contains the following blocking/conductive fracture surface integrals (taking into account the property of the Dirac-δ functions):

$$\boldsymbol{\Phi}_b(\boldsymbol{u}, \boldsymbol{v}) := \sum_{K \in \mathcal{T}_h^b} \sum_{i=1}^{M} \int_{K \cap \Gamma_{i,h}} \frac{\epsilon_i}{k_i} (\boldsymbol{u} \cdot \boldsymbol{n}_i)(\boldsymbol{v} \cdot \boldsymbol{n}_i) \, \mathrm{ds}, \tag{5e}$$

$$\boldsymbol{\Phi}_c(\boldsymbol{u}, \boldsymbol{v}) := \sum_{K \in \mathcal{T}_h^c} \sum_{i=M+1}^{M+N} \int_{K \cap \Gamma_{i,h}} \epsilon_i k_i (\boldsymbol{K}_m^{-1} \boldsymbol{u})_{t,i} \cdot (\boldsymbol{K}_m^{-1} \boldsymbol{v})_{t,i} \, \mathrm{ds}, \tag{5f}$$

where $(\boldsymbol{w})_{t,i} := \boldsymbol{w} - (\boldsymbol{w} \cdot \boldsymbol{n}_i)\boldsymbol{n}_i$ denotes the tangential component of a vector $\boldsymbol{w}$ on $\Gamma_{i,h}$, and the numerical flux $\widehat{\boldsymbol{u}}_h \cdot \boldsymbol{n}$ takes the following form:

$$\widehat{\boldsymbol{u}}_h \cdot \boldsymbol{n} := \boldsymbol{u}_h \cdot \boldsymbol{n} + \alpha_h (p_h - \widehat{p}_h), \tag{5g}$$

with $\alpha_h > 0$ being the stabilization function defined element-wise as follows:

$$\alpha_h|_K = \begin{cases} \boldsymbol{K}_m & \text{if } K \in \mathcal{T}_h^r, \\ C_b (h_K / L)^{s_b} \boldsymbol{K}_m & \text{if } K \in \mathcal{T}_h^r, \\ C_c \, (h_K / L)^{-s_c} \boldsymbol{K}_m & \text{if } K \in \mathcal{T}_h^c, \end{cases} \tag{5h}$$

where h_K is the local mesh size, L is the characteristic length of the domain Ω, and $C_b, C_c > 0$ and $s_b, s_c > 0$ are penalty parameters to be tuned. We note that proper tuning of these penalty parameters is important for the accuracy of the scheme (5); see Remark 2.4 below.

Remark 2.3 (*Connection with LDG-H for Regular Porous Media Flow*). In the absence of fractures ($\boldsymbol{\Phi}_b = \boldsymbol{\Phi}_c = 0$), we have $\widetilde{\boldsymbol{u}}_h = \boldsymbol{u}_h$ for the scheme (5). Hence, the scheme (5) reduces to the so-called LDG-H scheme introduced in Cockburn et al. (2009) and analyzed in Cockburn et al. (2010). In particular, the LDG-H scheme produces an optimal L^2-convergence rate of order h^{k+1} for the velocity approximation, and a superconvergent L^2-convergence rate of order h^{k+2} (under the usual full H^2-elliptic regularity assumption) for a special projection error of the pressure, from which a superconvergent postprocessed pressure approximation $p_h^* \in W_h^{k+1}$ can be constructed that satisfies

$$(\nabla p_h^*, \nabla q_h)_K = -(\boldsymbol{K}_m^{-1}\widetilde{\boldsymbol{u}}_h, \nabla q_h), \quad \forall q_h \in W_h^{k+1}, \quad \forall K \in \mathcal{T}_h, \tag{6a}$$

$$(p_h^*, 1)_K = (p_h, 1), \qquad \forall K \in \mathcal{T}_h. \tag{6b}$$

Scheme (5) is a novel modification of the classical LDG-H scheme by adding the fracture surface integrals $\boldsymbol{\Phi}_b$ and $\boldsymbol{\Phi}_c$ and adjusting the stabilization parameter α_h on conductive and blocking fractured cell. Hence, minimal amount of work is needed to convert a regular porous media flow HDG solver to a fractured porous media flow solver on unfitted meshes. This has to be contrasted with other fractured porous media flow models that model lower dimensional fractured flows where significant code re-design is needed (and are mostly restricted to geometrically fitted meshes); see, e.g. Alboin et al. (1999), Boon et al. (2018) and Fu and Yang (2022). In our numerical implementation reported in Section 3, we use the open-source finite-element software NGSolve (Schöberl, 2014) where the fracture surface integrals are realized using integration over domains defined by (multi-)level sets from the ngsxfem add-on (Lehrenfeld et al., 2021). Despite the simplicity of the scheme (5), its performance for various 2D and 3D benchmark examples reveal that it is also quite accurate.

We have the following well-posedness of the HDG scheme (5).

Theorem 2.1 (*Well-posedness*). *The solution to the HDG scheme (5) exists and is unique.*

Proof. Taking test functions $(\boldsymbol{v}_h, q_h, \widehat{q}_h) := (\boldsymbol{u}_h, p_h, \widehat{p}_h)$ in (5b)–(5d) and adding, we obtain the following identity:

$$(\boldsymbol{K}_m^{-1}\widetilde{\boldsymbol{u}}_h, \boldsymbol{u}_h)_{\mathcal{T}_h} + \langle \alpha_h(p_h - \widehat{p}_h), (p_h - \widehat{p}_h)\rangle_{\partial\mathcal{T}_h} = (f, \boldsymbol{u}_h)_{\mathcal{T}_h}. \tag{7}$$

Taking $\widetilde{\boldsymbol{v}}_h$ to be supported on a cell $K \in \mathcal{T}_h$ and using the definition of $\boldsymbol{\Phi}_b$ and $\boldsymbol{\Phi}_c$, we get

$$\begin{aligned}
(\boldsymbol{K}_m^{-1}\boldsymbol{u}_h, \widetilde{\boldsymbol{v}}_h)_K &= (\boldsymbol{K}_m^{-1}\widetilde{\boldsymbol{u}}_h, \widetilde{\boldsymbol{v}}_h)_K, && \forall K \in \mathcal{T}_h^r,\\
(\boldsymbol{K}_m^{-1}\boldsymbol{u}_h, \widetilde{\boldsymbol{v}}_h)_K + \boldsymbol{\Phi}_{b,K}(\boldsymbol{u}_h, \widetilde{\boldsymbol{v}}_h) &= (\boldsymbol{K}_m^{-1}\widetilde{\boldsymbol{u}}_h, \widetilde{\boldsymbol{v}}_h)_K, && \forall K \in \mathcal{T}_h^b,\\
(\boldsymbol{K}_m^{-1}\boldsymbol{u}_h, \widetilde{\boldsymbol{v}}_h)_K &= (\boldsymbol{K}_m^{-1}\widetilde{\boldsymbol{u}}_h, \widetilde{\boldsymbol{v}}_h)_K + \boldsymbol{\Phi}_{c,K}(\widetilde{\boldsymbol{u}}_h, \widetilde{\boldsymbol{v}}_h), && \forall K \in \mathcal{T}_h^c,
\end{aligned}$$

where $\boldsymbol{\Phi}_{b,K}$ and $\boldsymbol{\Phi}_{c,K}$ are restrictions of $\boldsymbol{\Phi}_b$ and $\boldsymbol{\Phi}_c$ on the respective cell K. Taking $\widetilde{\boldsymbol{v}}_h = \boldsymbol{u}_h$ on $K \in \mathcal{T}_h^r \cup \mathcal{T}_h^b$, and taking $\widetilde{\boldsymbol{v}}_h = \widetilde{\boldsymbol{u}}_h$ on $K \in \mathcal{T}_h^c$, we get

$$(\boldsymbol{K}_m^{-1}\boldsymbol{u}_h, \widetilde{\boldsymbol{u}}_h)_K = \begin{cases} (\boldsymbol{K}_m^{-1}\boldsymbol{u}_h, \boldsymbol{u}_h)_K & \text{if } K \in \mathcal{T}_h^r,\\ (\boldsymbol{K}_m^{-1}\boldsymbol{u}_h, \boldsymbol{u}_h)_K + \boldsymbol{\Phi}_{b,K}(\boldsymbol{u}_h, \boldsymbol{u}_h) & \text{if } K \in \mathcal{T}_h^b,\\ (\boldsymbol{K}_m^{-1}\widetilde{\boldsymbol{u}}_h, \widetilde{\boldsymbol{u}}_h)_K + \boldsymbol{\Phi}_{c,K}(\widetilde{\boldsymbol{u}}_h, \widetilde{\boldsymbol{u}}_h) & \text{if } K \in \mathcal{T}_h^c. \end{cases}$$

Combining the above equalities with identity (7) yields

$$E(\boldsymbol{u}_h, \widetilde{\boldsymbol{u}}_h) + \langle \alpha_h(p_h - \widehat{p}_h), (p_h - \widehat{p}_h)\rangle_{\partial\mathcal{T}_h} = (f, \boldsymbol{u}_h)_{\mathcal{T}_h},$$

where

$$E(\boldsymbol{u}_h, \widetilde{\boldsymbol{u}}_h) := (\boldsymbol{K}_m^{-1}\boldsymbol{u}_h, \boldsymbol{u}_h)_{\mathcal{T}_h^r \cup \mathcal{T}_h^b} + (\boldsymbol{K}_m^{-1}\widetilde{\boldsymbol{u}}_h, \widetilde{\boldsymbol{u}}_h)_{\mathcal{T}_h^c} + \boldsymbol{\Phi}_b(\boldsymbol{u}_h, \boldsymbol{u}_h) + \boldsymbol{\Phi}_c(\widetilde{\boldsymbol{u}}_h, \widetilde{\boldsymbol{u}}_h)$$

is non-negative.

Now let us establish uniqueness of the solution using the above energy identity. Taking $f = 0$, we have

$$E(\boldsymbol{u}_h, \widetilde{\boldsymbol{u}}_h) = 0, \text{ and } \langle \alpha_h(p_h - \widehat{p}_h), (p_h - \widehat{p}_h)\rangle_{\partial\mathcal{T}_h} = 0,$$

which implies that $p_h = \widehat{p}_h$ on $\partial\mathcal{T}_h$, $\boldsymbol{u}_h = 0$ on $\mathcal{T}_h^r \cup \mathcal{T}_h^b$, and $\widetilde{\boldsymbol{u}}_h = 0$ on $\mathcal{T}_h^c$. Eq. (5a) then implies that $\widetilde{\boldsymbol{u}}_h = \boldsymbol{u}_h = 0$ on all cells. And Eq. (5b), together with $p_h = \widehat{p}_h$, implies that $\nabla p_h = 0$. Hence p_h is a global constant. Using the homogeneous Dirichlet boundary condition on $\widehat{p}_h$, we conclude that $p_h = 0$ and $\widehat{p}_h = 0$. Hence we proved the uniqueness. Existence of the solution is a direct consequence of uniqueness as the system (5) is a square linear system. □

Remark 2.4 (*On the Stabilization Function*). In practice (see Section 3 below), we found taking $s_c \geq 3$ in (5h) leads to a convergent scheme for polynomial degree $k \geq 1$, while taking $s_c < 3$ may produce large consistency errors on conductive fractures. This indicates the stabilization needs to be very large on conductive fractures. The reason for such large choice of stabilization is to implicitly enforce the pressure continuity across the boundary of conductive fractured cells as the physical model has such continuity while the surface integral $\boldsymbol{\Phi}_c$ on conductive fractures itself does not enforce such pressure continuity. Equally well, the choice of smaller stabilization (with $s_b > 0$) in (5h) on blocking fractured cells has the effect of enforcing the velocity normal continuity across the boundary of blocking fractured cells to be consistent with the physical model. Here we found that when $\epsilon_i/k_i \approx \boldsymbol{K}_m^{-1}$ for blocking fractures, we can simply use the same stabilization on blocking cells as those on the regular cells, i.e., with $C_b = 1$ and $s_b = 0$; see Examples 1 and 2 in Section 3. On the other hand, when $\epsilon_i/k_i \gg \boldsymbol{K}_m^{-1}$, we need to reduce the blocking cell stabilization to enforce the normal velocity continuity, where taking $C_b = 1$ and $s_b = 2$ usually gives a good result; see Examples 3 and 6 in Section 3.

Here we provide another heuristic argument to justify the large stabilization on conductive fractures. We assume permeability $\boldsymbol{K}_m$ is a constant on each cell K in the following discussion. Taking $\alpha_h|_K \to \infty$ on conductive fractures, we have $p_h \approx \widehat{p}_h$ on ∂K for all $K \in \mathcal{T}_h^c$ under the reasonable assumption that the numerical flux $\widehat{\boldsymbol{u}}_h \cdot \boldsymbol{n}$ stays bounded. Then Eq. (5b) implies that $\widetilde{\boldsymbol{u}}_h \approx -\boldsymbol{K}_m\nabla p_h$. Taking $\widetilde{\boldsymbol{v}}_h := \boldsymbol{K}_m\nabla q_h$ on $\mathcal{T}_h^c$ in (5a) with $q_h \in W_h$ that is continuous across interior facets of $\mathcal{T}_h^c$, we have

$$\begin{aligned}
-(\boldsymbol{u}_h, \nabla q_h)_{\mathcal{T}_h^c} &= -(\widetilde{\boldsymbol{u}}_h, \nabla q_h)_{\mathcal{T}_h^c} - \boldsymbol{\Phi}_c(\widetilde{\boldsymbol{u}}_h, \boldsymbol{K}_m\nabla q_h)\\
&\approx (\boldsymbol{K}_m\nabla p_h, \nabla q_h)_{\mathcal{T}_h^c} + \boldsymbol{\Phi}_c(\boldsymbol{K}_m\nabla p_h, \boldsymbol{K}_m\nabla q_h),
\end{aligned}$$

Combine the above relation with (5c) and using the fact that q_h is continuous across interior facets of $\mathcal{T}_h^c$, we get

$$(\boldsymbol{K}_m\nabla p_h, \nabla q_h)_{\mathcal{T}_h^c} + \boldsymbol{\Phi}_c(\boldsymbol{K}_m\nabla p_h, \boldsymbol{K}_m\nabla q_h) \approx (f, q_h)_{\mathcal{T}_h^c} - \langle \widehat{\boldsymbol{u}}_h \cdot \boldsymbol{n}, q_h\rangle_{\Gamma_h^c},$$

where Γ_h^c is the exterior boundary of $\mathcal{T}_h^c$. The above relation show that p_h will be a good approximation to the H^1-conforming finite element discretization of the RDFM model on conductive fractures (Fu and Yang, 2022), which was known to provide a consist approximation with respect to the conductive fractures as long as W_h contains at least piecewise linear functions.

The lowest-order case with $k = 0$ requires further attention. It is more subtle to find a good set of penalty parameters on conductive fractured cells for $k = 0$. If it is taking to be too large, the strong penalty will effectively makes pressure along fractures to be a global constant, leading to large consistency errors. On the other hand, if the stabilization is taking to be too small, the effects of conductive fractures will not be seen by the scheme. Our numerical experiments below suggests that taking $s = 2$ for $k = 0$ may lead to reasonable approximations.

We will investigate more on the effects of the stabilization function on the HDG scheme in our future work.

Remark 2.5 (*Hybrid-mixed Methods*). We can increase the velocity space $\boldsymbol{V}_h^k$ to be a discontinuous Raviart–Thomas space of degree k:

$$\boldsymbol{V}_h^{RT,k} := \{\boldsymbol{v} \in [L^2(\mathcal{T}_h)]^d : \boldsymbol{v}|_K \in [P_k(K)]^d \oplus \boldsymbol{x}\widetilde{P}_k(K), \quad \forall K \in \mathcal{T}_h\},$$

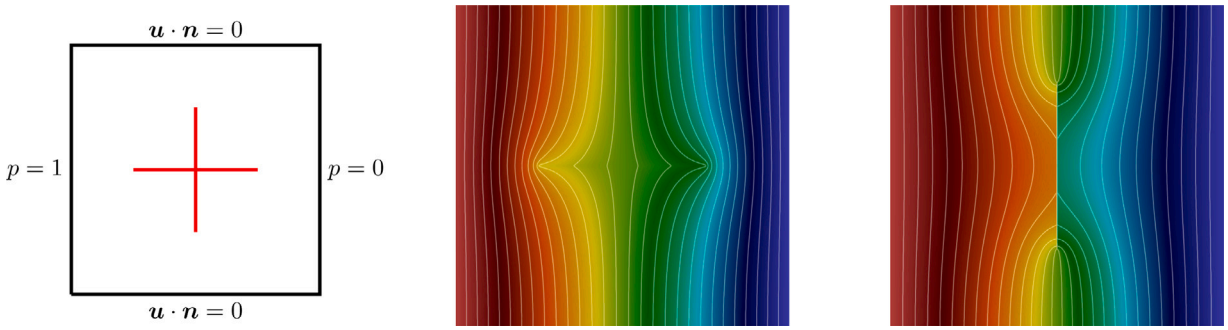

Fig. 1. Example 1. Left: Domain and boundary conditions. Middle: reference solution for conductive fractures (1a). Right: reference solution for blocking fractures (1b). Color range: (0, 1). Thirty uniform contour lines from 0 to 1.

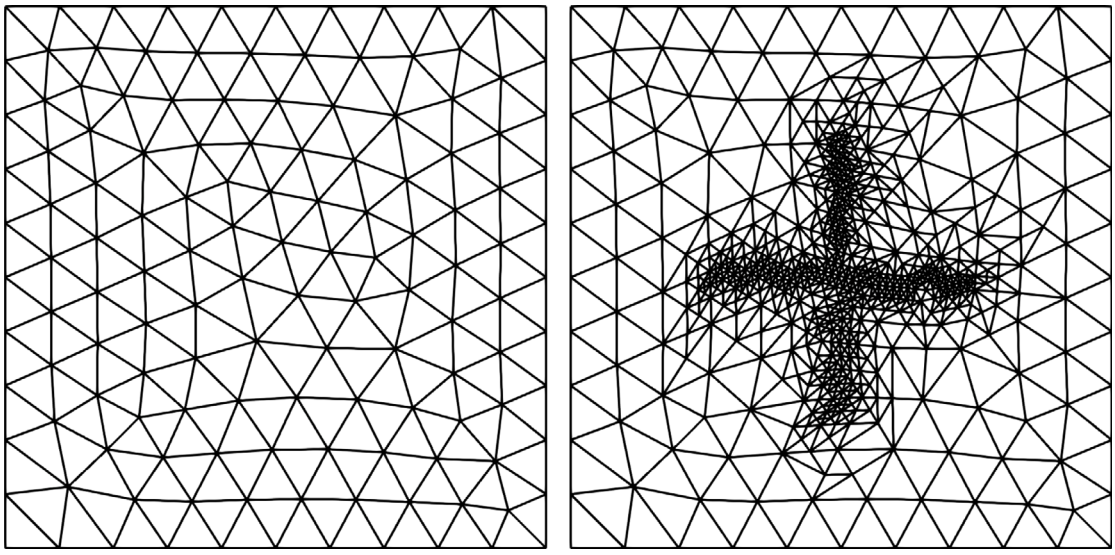

Fig. 2. Example 1. Left: a coarse mesh with size $h = 0.1$. Right: a locally refined mesh with $h \approx 0.1/8$ near the fractures.

where $\widetilde{P}_k(K)$ is the space of homogeneous polynomials of degree k. Then the velocity-pressure pair $\boldsymbol{V}_h^{RT,k}$ and W_h^k satisfy the inf-sup condition, and we can set the stabilization α_h on $\mathcal{T}_h^r \cup \mathcal{T}_h^b$ to be zero when using $\boldsymbol{V}_h^{RT,k}$, W_h^k, and M_h^k in the scheme (5) (while still keep the large stabilization on conductive fractures). The resulting scheme is the hybrid-mixed method, whose computational cost is similar to the HDG scheme (5). We note that the lowest-order hybrid-mixed method for porous media containing pure blocking fractures was already introduced in our earlier work (Fu and Yang, 2022).

Remark 2.6 (*Variable Polynomial Degree on Different Cells*)**.** The large stabilization on conductive fractures may lead to less accurate velocity approximations therein since $\boldsymbol{u}_h \approx -\boldsymbol{K}_m^{-1}\nabla p_h$. An interesting variant of the scheme is to use one degree higher on conductive fractured cells $\mathcal{T}_h^c$ than those on regular and blocking fractured cells, that is, replacing the spaces $\boldsymbol{V}_h^k, W_h^k$ and M_h^k in (5) by the following reduced version:

$$\boldsymbol{V}_h^{k-1,k} := [W_h^{k-1,k}]^d, \tag{8a}$$

$$W_h^{k-1,k} := \{w \in W_h^k : \ w|_K \in P_{k-1}(K), \quad \forall K \in \mathcal{T}_h^r \cup \mathcal{T}_h^b\}, \tag{8b}$$

$$M_h^{k-1,k} := \{\mu \in M_h^k : \ \mu|_F \in P_{k-1}(F), \quad \forall F \in \mathcal{E}_h \text{ with } F \cap \partial\mathcal{T}_h^c = \emptyset\}. \tag{8c}$$

This reduced version is less accurate than the original version but is cheaper to solve as it has less DOFs.

In this work, we present numerical results only for the original HDG scheme (5) with polynomial degree $k = 0, 1, 2$. We will explore the performance of the above mentioned hybrid-mixed method and variable-degree variants in our future work.

Remark 2.7 (*Static Condensation and Efficient Implementation*)**.** Just like the LDG-H scheme for regular porous media flow, we can solve system (5) efficiently using static condensation where one first locally eliminates the cell-wise DOFs to express the unknowns $\widetilde{\boldsymbol{u}}_h, \boldsymbol{u}_h, p_h$ as (local) functions of the global unknown $\widehat{p}_h$ and source term f using (5a)–(5c), and then solve the global transmission problem (5d) for $\widehat{p}_h$, which is a sparse and symmetric positive definite linear system whose efficient solution procedure can be designed following similar work for regular porous media flows; see, e.g., Cockburn et al. (2014), Fu (2021).

Remark 2.8 (*Local Mesh Refinement Near Fractures*)**.** Since the computational mesh $\mathcal{T}_h$ is assumed to be completely independent of the fractures, the approximation quality of the scheme (5) on an initial coarse mesh that does not know the fracture locations may be poor. Here we propose to use local mesh refinement that only refine cells intersected by the fractures. In particular, given an initial mesh $\mathcal{T}_h := \mathcal{T}_h^r \cup \mathcal{T}_h^b \cup \mathcal{T}_h^c$, we only mark cells in $\mathcal{T}_h^b$ and $\mathcal{T}_h^c$ for refinement using the bisection algorithm. Multiple refinements can be performed sequentially as needed. This refinement procedure puts more cells around fractures and leads to significantly more efficient algorithms comparing with a naïve uniform refinement procedure.

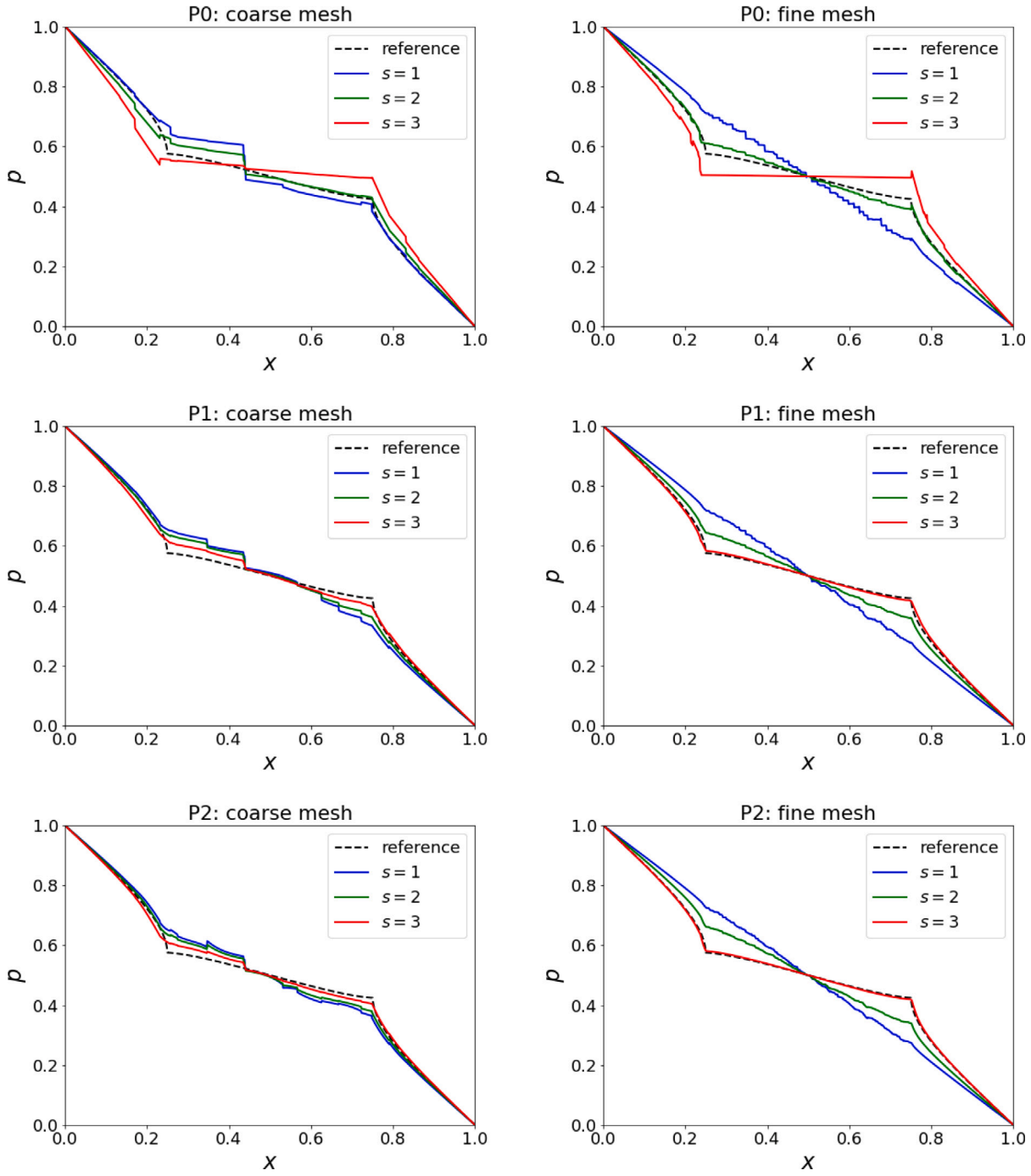

Fig. 3. Example 1(a): conductive fractures. Pressure along cut line $x = 0.5$ for the scheme (5) with different stabilization parameter with $s_c = s = 1, 2, 3$ in (5h).

3. Numerical examples

In this section, we present detailed numerical results in two and three dimensions for the proposed HDG scheme (5). When evaluating pressure distribution along line segments, we always evaluate the postprocessed pressure approximation (6). Our numerical simulations are performed using the open-source finite-element software NGSolve (Schöberl, 2014), https://ngsolve.org/. In particular, the (multi-)level set representation of the fractures and their associated surface integrations are realized using the ngsxfem add-on (Lehrenfeld et al., 2021). Sample code can be found in the git repository https://github.com/gridfunction/fracturedPorousMedia. Specifically, two jupyter notebook files, complex2D-HDG.ipynb (for Example 2) and single3Dhex-HDG.ipynb (for Example 4), are included in this git repository, which can be executed using the provided binder therein without local installation.

Example 1 (*Cross-shaped Fractures in 2D*)**.** In this example, we test the performance of the scheme (5) for a fractured media with simple cross-shaped fractures. Similar test was used in Tene et al. (2017). The computational domain is a unit square $\Omega = [0, 1] \times [0, 1]$. Two fractures with thickness $\epsilon = 10^{-3}$ and length 0.5 are located in the region given below and cross each other at the center $(0.5, 0.5)$:

$$\Gamma_1 = \{(x, 0.5) : 0.25 \le x \le 0.75\}, \quad \Gamma_2 = \{(0.5, y) : 0.25 \le y \le 0.75\}.$$

The matrix permeability is $\boldsymbol{K}_m = 1$ and the fracture permeability is either (a) $k_1 = k_2 = 10^3$ for the conductive case or (b) $k_1 = k_2 = 10^{-3}$

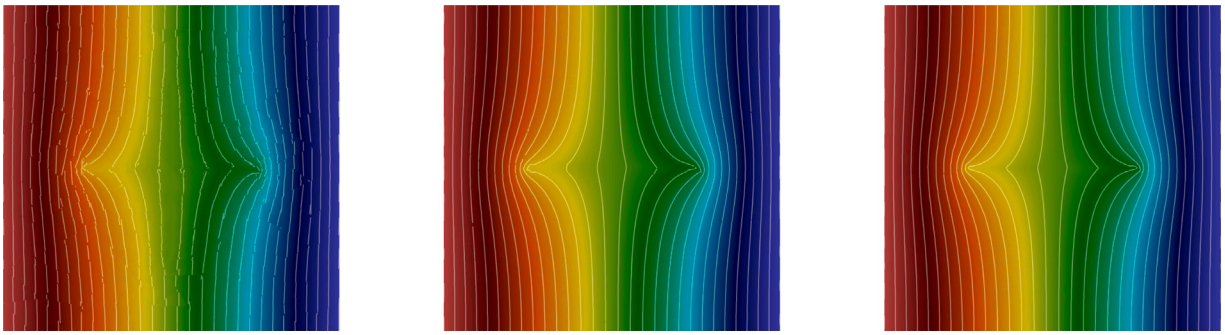

Fig. 4. Example 1(a): conductive fractures. Pressure contour for $k = 0, s = 2$ (left), $k = 1, s = 3$ (middle), and $k = 2, s = 3$ (right).

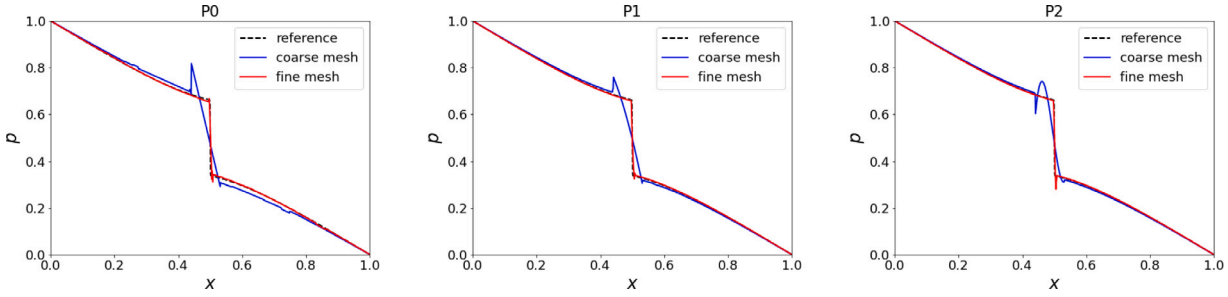

Fig. 5. Example 1(b): Pressure along cut line $x = 0.5$ for the scheme (5) for the blocking fracture case.

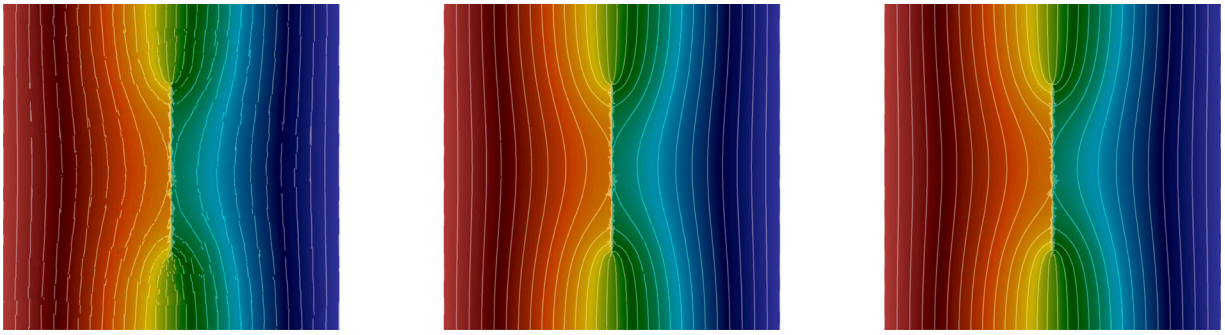

Fig. 6. Example 1(b): Pressure contour for $k = 0$ (left), $k = 1$ (middle), and $k = 2$ (right).

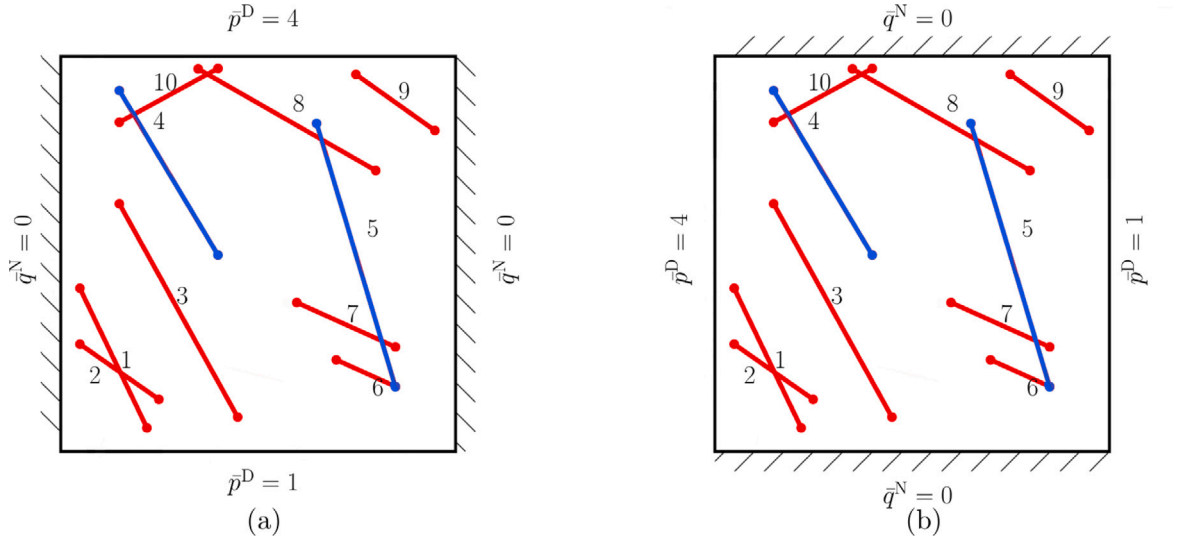

Fig. 7. Benchmark 3: computational domain and boundary conditions.

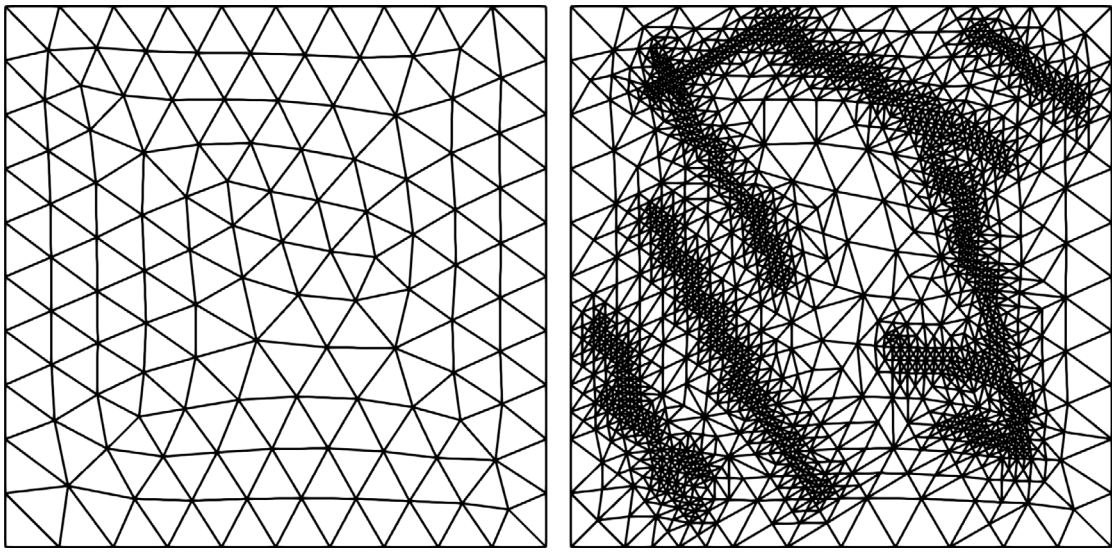

Fig. 8. Example 2. Left: a coarse mesh with size $h = 0.1$. Right: a locally refined mesh with $h \approx 0.1/8$ near the fractures.

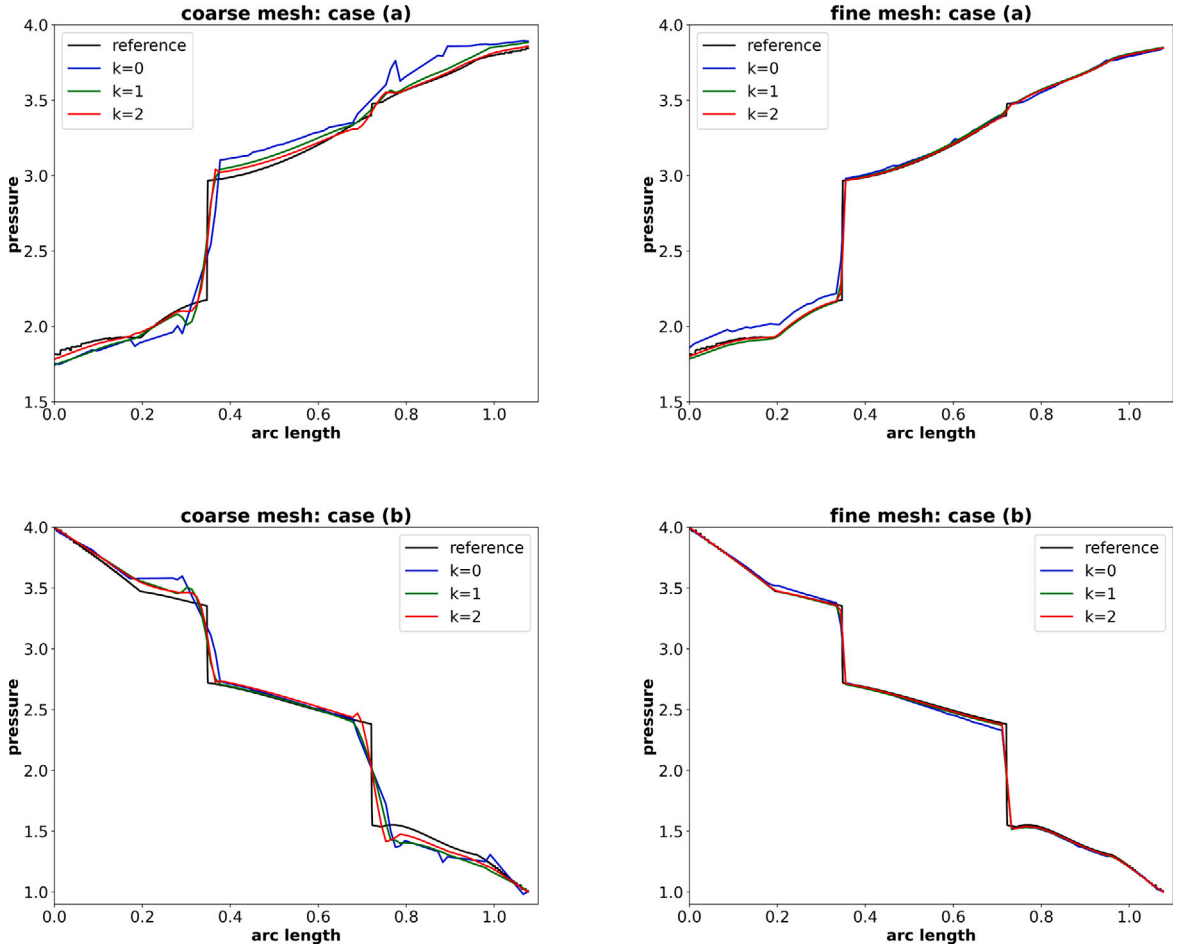

Fig. 9. Example 2. Pressure along line segment $(0, 0.5) - -(1, 0.9)$ for the scheme (5) on two meshes. Top row: case (a); Bottom row: case (b).

for the blocking case. Source term is $f = 0$, and the problem is closed with no flow boundary condition on the top and bottom boundaries and Dirichlet boundary condition $p = 1$ on the left boundary and $p = 0$ on the right boundary. See Fig. 1 for an illustration of the setup and the reference solutions for the two cases. Here the reference solutions are obtained using a continuous Q_1 finite element scheme on a uniform 2000×2000 rectangular mesh where the fracture has been fully resolved.

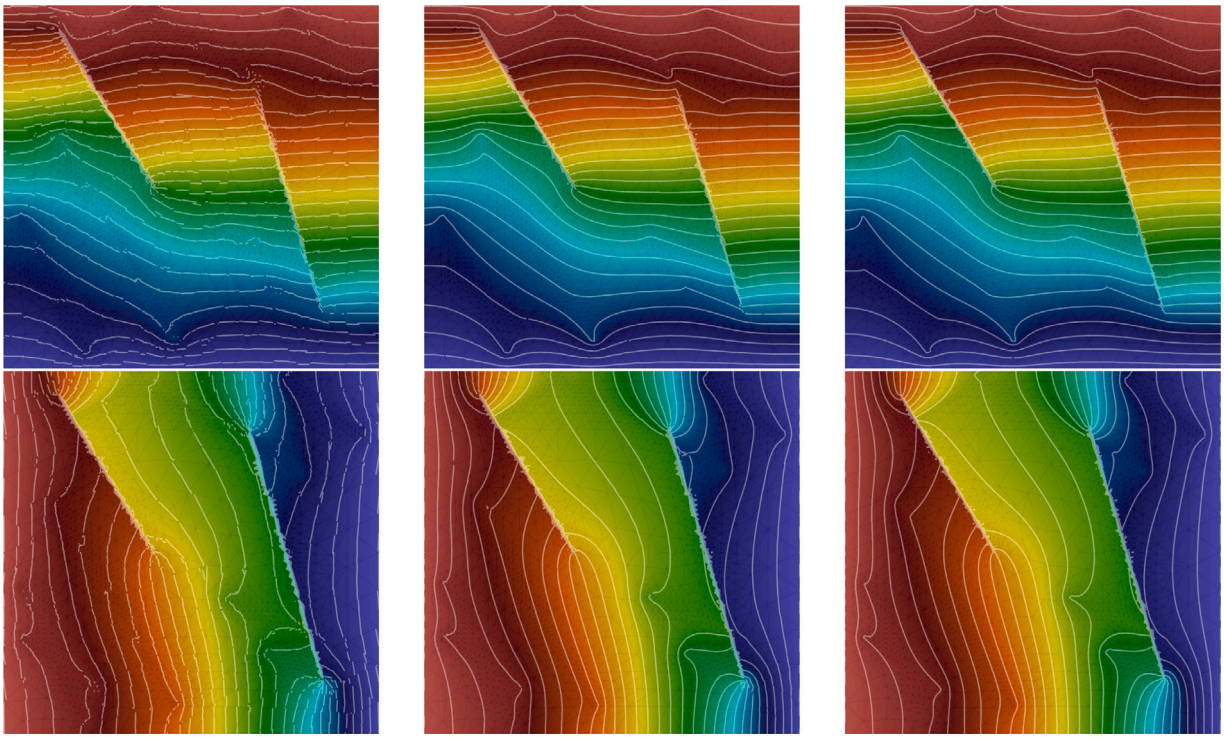

Fig. 10. Example 2. Pressure contour for $k = 0$ (left), $k = 1$ (middle), and $k = 2$ (right). Color range: (0,1). Thirty uniform contour lines from 0 to 1.

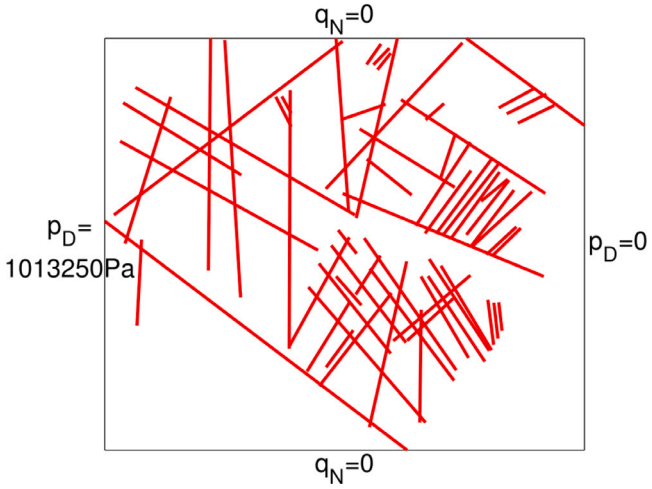

Fig. 11. Example 3: Computational domain and boundary conditions.

We consider two meshes, see Fig. 2: a coarse unfitted triangular mesh with mesh size $h = 0.1$ and a refined unfitted mesh that performs 3 steps of local mesh refinements near the fractured cells using the procedure detailed in Remark 2.8. The coarse mesh has 230 cells, while the fine mesh has 1328 cells.

We first study the role of the stabilization function α_h, in particular, the effect of s_c therein, near conductive fractures on the scheme (5). We take polynomial degree $k = 0, 1, 2$, and vary the scaling power $s_c \in \{1, 2, 3\}$ of α_h in (5h) with $C_c = 1$. The pressure approximations along the line $x = 0.5$ are shown in Fig. 3. From these figures, we observe that

- When polynomial degree $k = 0$, a convergent result, comparing with the reference solution, is obtained with $s = 2$. For $s = 1$ (smaller stabilization) the scheme does not converge as the fracture is not captured. For $s = 3$ (larger stabilization) the scheme does not convergence either as it leads to a constant approximation along the fractures, which is consistent with the discussion in Remark 2.4 as too large stabilization effectively makes the pressure within conductive fractures to be a global constant for $k = 0$.
- When polynomial degree $k = 1$ or $k = 2$, a convergent result is obtained with $s = 3$. The results for $s = 1$ and $s = 2$ leads to locking phenomena as the effects of the fracture is not captured correctly. We note that further increasing s from 3 essentially leads to similar results as those with $s = 3$ for this example.

Contour plots of the pressure on the fine mesh for $k = 0$ with $s_c = 2$ and for $k = 1, 2$ with $s_c = 3$ are shown in Fig. 4. We observe these results are qualitatively similar to the reference solution in the middle of Fig. 2.

We next study the performance of our scheme for the blocking fracture case. For this case, we find that taking the penalty parameter on blocking fractured cells to be the same as regular cells (i.e., $C_b = 1$ and $s_b = 0$) already lead to a convergent scheme, so we only report results for this choice of parameters. The pressure approximations along the line $x = 0.5$ for $k = 0, 1, 2$ on the coarse and fine meshes are shown in Fig. 5. Convergence to the reference solution is observed for all cases as mesh refines. Here we can also observe some overshoot and undershoot (around $x = 0.5$), which is mainly due to the unfitted meshes used in the numerical simulations and the reference solution has a jump discontinuity in pressure around $x = 0.5$. Contour plots of the pressure on the fine mesh are shown in Fig. 6. We again observe these results are qualitatively similar to the reference solution on the right of Fig. 2.

Example 2 (*Complex Fracture Network in 2D*)**.** This test case considers a small but complex fracture network that includes eight conductive fractures and two blocking fractures. The domain and boundary conditions are shown in Fig. 7 (red represents conductive fractures, blue represents blocking fractures). All fractures are represented by line segments, and the exact coordinates for the fracture positions can be found in Flemisch et al. (2018, Appendix C). The fracture thickness is $\epsilon = 10^{-4}$ for all fractures, and permeability is $k_i = 10^4$ for all fractures

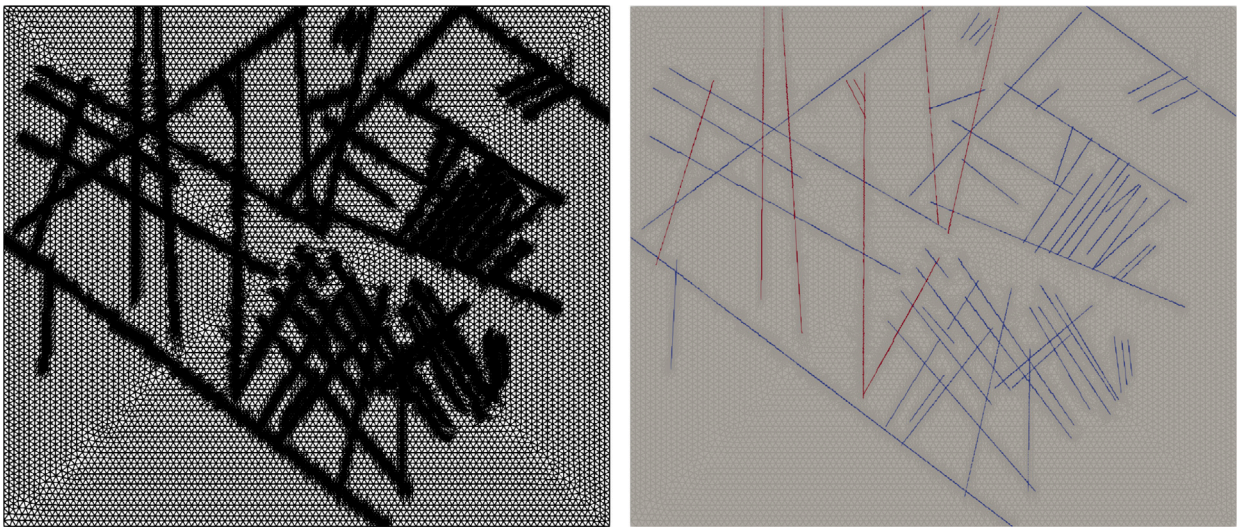

Fig. 12. Example 3. Left: unfitted mesh with 154,174 cells. Right: location of blocking (in red) and conductive (in blue) fractured cells for case (c).

except for fractures 4 and 5 which are blocking fractures with $k_i = 10^{-4}$. We consider two subcases (a) and (b) with a pressure gradient which is predominantly vertical and horizontal respectively. As discussed in Remark 2.2, we do not include the conductive fracture segment in a computational cell that contains both conductive and blocking fracture segments into in the HDG formulation (5).

We consider two meshes, see Fig. 8: a coarse triangular mesh with mesh size $h = 0.1$ and a refined mesh that performs 3 steps of local mesh refinements near the fractures using the procedure detailed in Remark 2.8. The coarse mesh has 230 cells, while the fine mesh has 1380 cells.

We take polynomial degree $k = 0, 1, 2$. As suggested from the previous example, we take penalty parameters $C_b = C_c = 1$ and $s_b = 0$, and use $s_c = 2$ if $k = 0$ and $s_c = 3$ if $k = 1, 2$. The quantity of interest is the pressure approximation along the line segment $(0, 0.5) - -(1, 0.9)$ for both cases, which are recorded in Fig. 9. We observe a good convergence towards the reference solution as mesh refines for all cases. Contour plots of the pressure on the fine mesh are shown in Fig. 10, which are consist with the results in the literature (Flemisch et al., 2018).

Example 3 (*A Realistic Case in 2D*)**.** We consider a real set of fractures from an interpreted outcrop in the Sotra island, near Bergen in Norway. The setup is adapted from Flemisch et al. (2018, Benchmark 4). The domain along with boundary conditions is given in Fig. 11. The size of the domain is 700 m × 600 m with uniform scalar permeability $\mathbb{K}_m = 10^{-14}$ m^2. The set of fractures is composed of 63 line segments with thickness $\epsilon = 10^{-2}$ m^2. The exact coordinates for the fracture positions are provided in the git repository https://git.iws.uni-stuttgart.de/benchmarks/fracture-flow. Three subcases will be considered: (a) all conductive fractures with permeability $k_c = 10^{-8}$ m^2, (b) all blocking fractures with permeability $k_b = 10^{-20}$ m^2, and (c) 9 blocking fractures with $k_b = 10^{-20}$ m^2 and 54 conductive fractures with $k_c = 10^{-8}$ m^2. Location of the blocking/conductive fractures for case (c) are marked in red/blue in the right panel of Fig. 12. We note that while case (a) has been extensively studied, see e.g. Flemisch et al. (2018). The other two cases are new.

Here we run simulation on a non-dimensional setting to avoid extreme values where the domain is scaled back to be $\Omega = (0, 1) \times (0, 6/7)$, matrix permeability $\mathbb{K}_m = 1$, and inflow pressure boundary condition $p_D = 1$ on the left boundary. We consider our scheme (5) with polynomial degree $k = 0, 1, 2$ on an unfitted mesh obtained from a uniform triangular mesh with $h = 0.01$ by performing two steps of local mesh refinements around the fractured cells; see left of Fig. 12. The mesh has about $154k$ total triangular cells, and about $27.5k$ fractured cells, which further split to $5.5k$ blocking fractured cells and $22k$ conductive fractured cells for case (c). The penalty parameters in (5h) are given in Table 1. Here due to stronger conductive/blocking effects (with permeability differs by six orders of magnitude), we need to choose the penalty parameters s_b and C_c differently than the previous two examples. In particular, we note that the C_c values are tuned to make the case (a) results matching with existing work. Moreover, the stabilization on blocking fractured cells are reduced by taking $s_b = 2$, as taking larger stabilization with $s_b = 0$ leads to pressure leakage across blocking fractured cells.

Table 1
Example 3. Choice of the penalty parameters for different polynomial degree k.

k	C_b	s_b	C_c	s_c
0	1	2	6	2
1	1	2	0.08	3
2	1	2	0.16	3

The pressure approximations along the two lines $y = 5/7$ and $x = 625/700$ are recorded in Fig. 13, where reference data from the Mortar-DFM scheme on a fitted mesh with about $10k$ cells reported in Flemisch et al. (2018) for case (a) is also presented. We observe a good agreement with the reference data for case (a) for our schemes. Moreover, we observe very close results for $k = 1$ and $k = 2$ for case (b) and case (c), where the results for $k = 0$ is slightly off due to coarse mesh resolution and low-order approximations. Further refining the mesh for $k = 0$ leads to results closer to the $k = 1, 2$ cases in Fig. 13.

Contour plots of the pressure are shown in Fig. 14, where the case (a) results are again consist with those in the literature (Flemisch et al., 2018). We also clearly observe the blocking effects (with discontinuous pressures) of the fractures for case (b), and the combined conductive/blocking effects of the fractures for case (c). This example confirms the ability of the proposed HDG scheme (5) in simulating realistic complex fracture networks on unfitted meshes with both conductive and blocking fractures.

Example 4 (*Single Fracture in 3D*)**.** This is the first 3D benchmark case proposed in Berre et al. (2021). The matrix domain $\Omega = (0, 100) \times (0, 100) \times (0, 100)$ which is crossed by a conductive planar fracture Γ_1 connected by the points $(0, 0, 80)$, $(100, 0, 20)$, $(100, 100, 20)$, $(0, 100, 80)$ with a thickness of $\epsilon = 10^{-2}$. The matrix permeability is heterogeneous and is taken to be $\boldsymbol{K}_m = 10^{-6}$ when $z \geq 10$ and $\boldsymbol{K}_m = 10^{-5}$ when $z < 10$.

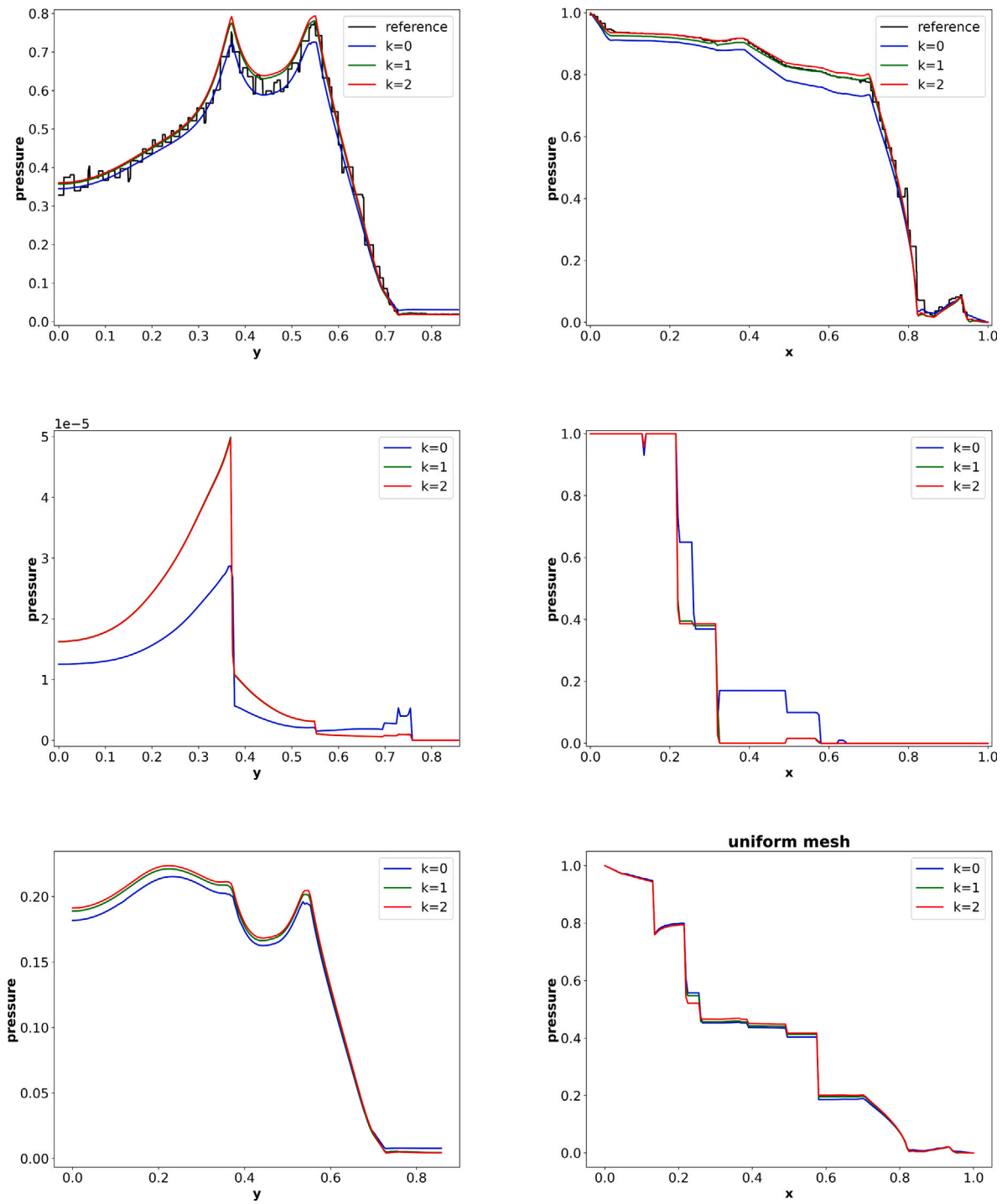

Fig. 13. Example 3. Pressure along line $y = 5/7$ (left column) and along line $x = 625/700$ (right column). Here reference data for case (a) is the result for the Mortar-DFM scheme in Flemisch et al. (2018).

The fracture conductivity is $k_c = 0.1$ so that $\epsilon k_c = 10^{-3}$. We apply the Dirichlet boundary conditions on the two boundaries

$$\Gamma_{in} := \{0\} \times (0, 100) \times (90, 100), \Gamma_{out} := (0, 100) \times \{0\} \times (0, 10),$$

where $p = 4$ on Γ_{in} and $p = 1$ on Γ_{out}. No flow boundary conditions is used on the rest of the domain boundary.

In this example, we apply the HDG scheme (5) with degree $k = 0, 1, 2$ on two uniform hexahedral meshes with mesh size $h = 10$ (1000 cubic cells) and $h = 5$ (8000 cubic cells) where we take $s_c = 2$ and $C_c = 1$ for $k = 0$, and $s_c = 3$ and $C_c = 1$ for $k = 1, 2$ in the stabilization parameters. Here the characteristic length in (5h) is $L = 100$. We plot in Fig. 15 pressure along the diagonal line $(0, 0, 0) - (100, 100, 100)$ together with reference data provided in Berre et al. (2021) which is obtained from the USTUTT-MPFA method therein on a mesh with approximately 1 million matrix elements. Good agreement with reference solution is observed for $k = 1$ and $k = 2$. The results for $k = 0$ is slightly off, but it improves as mesh refines.

Example 5 (*Network with Small Features in 3D*)**.** This is the third benchmark case proposed in Berre et al. (2021), in which small geometric features exist. The domain is the box $\Omega = (0, 1) \times (0, 2.25) \times (0, 1)$, containing 8 planer conductive fractures; see Fig. 16. Homogeneous

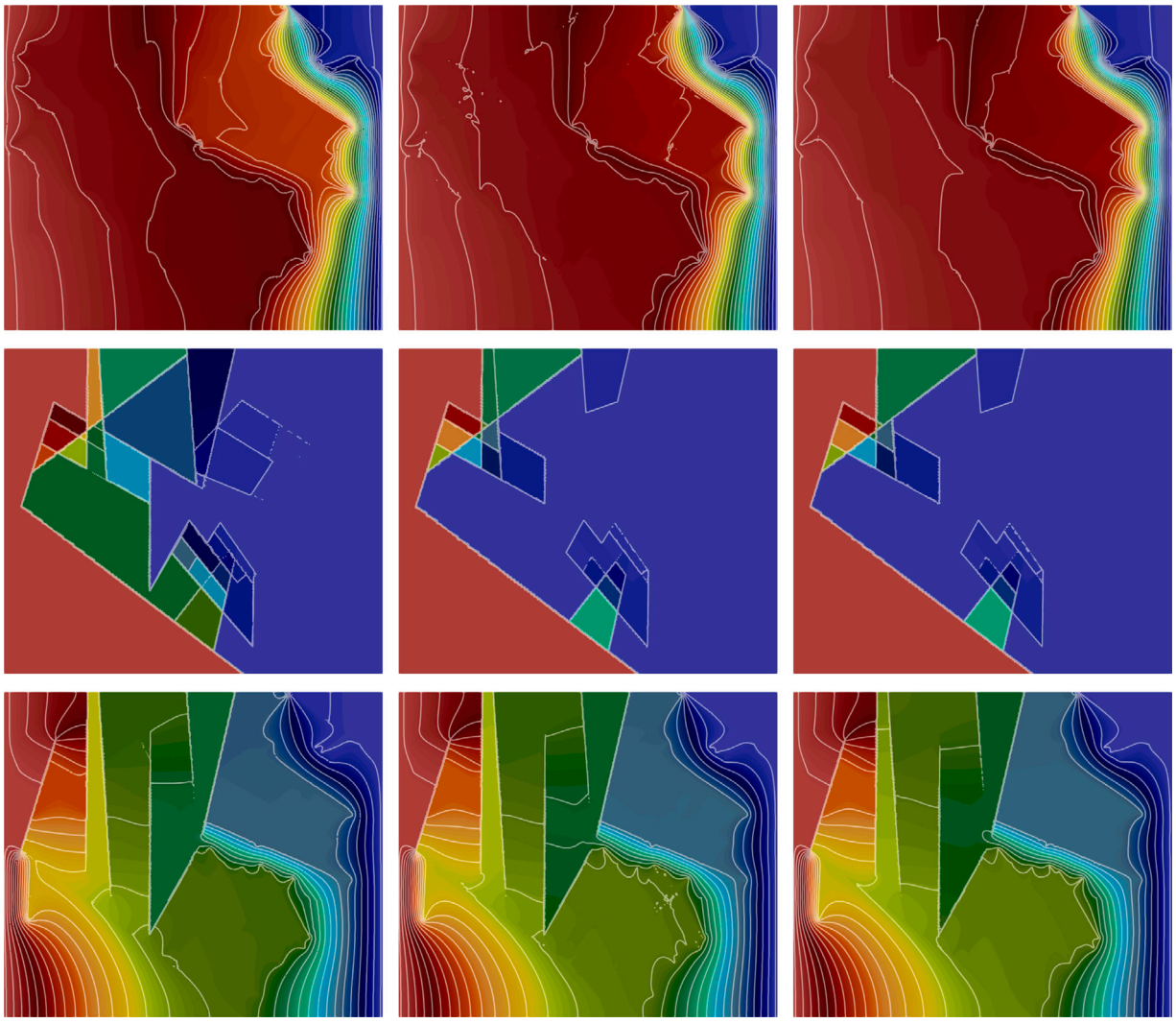

Fig. 14. Example 3. Pressure contours for $k = 0$ (left), $k = 1$ (middle), and $k = 2$ (right). Top row: case (a). Middle row: case (b). Bottom row: case (c). Color range: (0,1). Thirty uniform contour lines from 0.01 to 0.99.

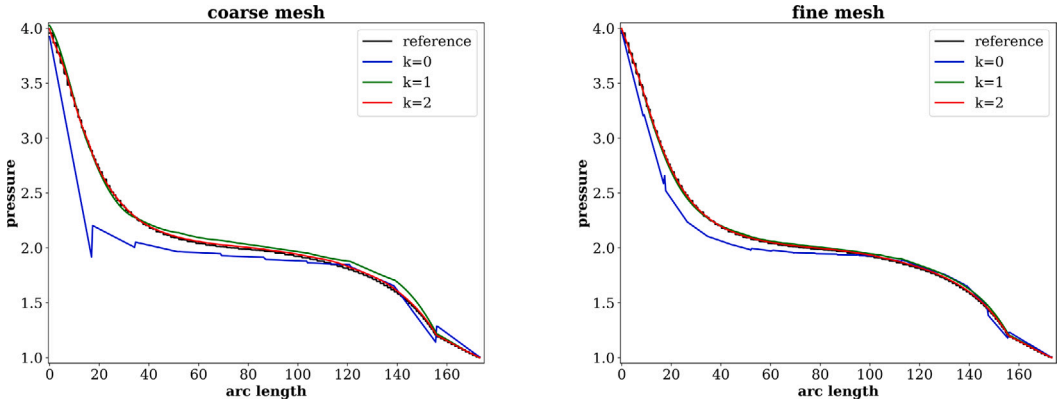

Fig. 15. Example 4. Pressure along line $(0,0,0) - -(100,100,100)$. Here reference data is the result from the USTUTT-MPFA scheme in Berre et al. (2021) on a mesh with roughly 1 million matrix elements.

Dirichlet boundary condition is imposed on the outlet boundary

$$\partial\Omega_{out} := \{(x,y,z) : 0 < x < 1, y = 2.25, z < 1/3 \text{ or } z > 2/3\},$$

inflow boundary condition $\boldsymbol{u} \cdot \boldsymbol{n} = -1$ is imposed on the inlet boundary

$$\partial\Omega_{in} := \{(x,y,z) : 0 < x < 1, y = 0, 1/3 < z < 2/3\},$$

and no-flow boundary condition is imposed on the remaining boundaries. The permeability in the matrix is $\mathbb{K}_m = 1$, and that in the fracture is $k_c = 10^4$. Fracture thickness is $\epsilon = 0.01$. The locations of these 8 fractures can be found in the git repository https://git.iws.uni-stuttgart.de/benchmarks/fracture-flow-3d where a sample gmsh geometric file was also provided. This problem is very challenging due to the small

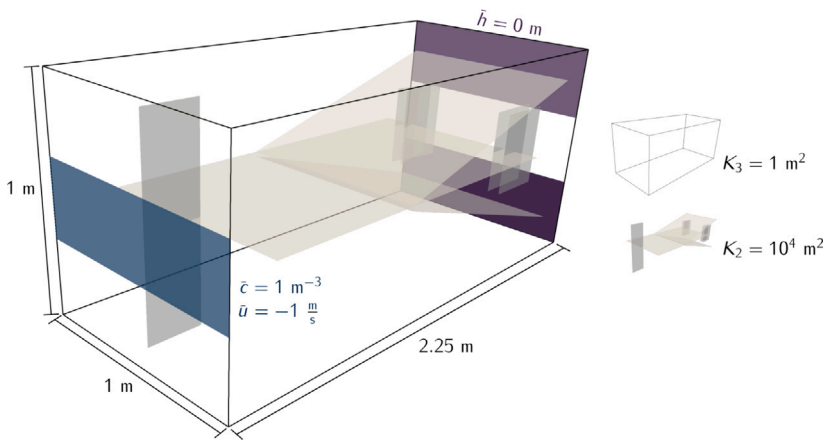

Fig. 16. Example 5: Conceptual model and geometrical description of the domain.

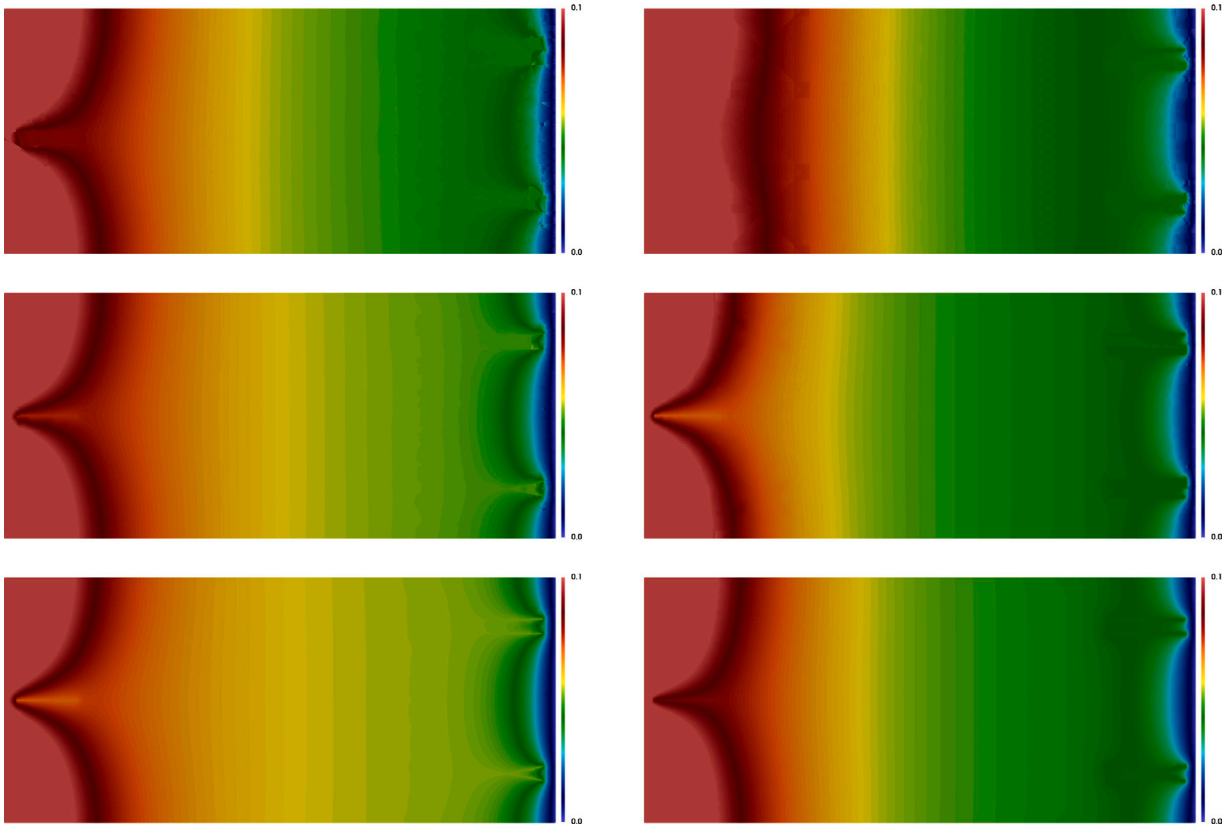

Fig. 17. Example 5. Pressure contour on the plane $z = 0.7$ for $k = 0$ (top), $k = 1$ (middle), and $k = 2$ (bottom). Left: fitted mesh ($\tilde{1}$48k cells). Right: unfitted mesh ($\tilde{1}$32k cells).

intersections among the fractures exist. The reported works in Berre et al. (2021) showed large discrepancies among the 16 participating methods.

Here we run simulations for the scheme (5) with $k = 0, 1, 2$ on two meshes: a fitted mesh with about 148k tetrahedral cells obtained from the above mentioned gmsh file with maximal mesh size $h \approx 0.074$ and minimal mesh size $h \approx 0.01$, and an unfitted mesh with about 132k tetrahedral cells obtained from local mesh refinements of a coarse uniform mesh near the fractures with maximal mesh size $h \approx 0.26$ and minimal mesh size $h \approx 0.026$. The penalty parameters for polynomial degree $k = 0, 1, 2$ on these two meshes are shown in Table 2, where the characteristic length $L = 2.25$. We first show the pressure contours along the plane $z = 0.7$ which intersects with 6 fractures in Fig. 17, from which we observe large variations among the results on the two meshes, especially for $y \geq 1$ where the fractures near the outlet starts to interact with the flow. This observation is in line with the findings in Berre et al. (2021) where significant difference among participating methods were reported for the pressure distribution along the center line $(0.5, 1.1, 0) - (0.5, 1.1, 1.0)$, suggesting that the small features of the fracture network geometry may be not adequately resolved on these meshes. We also plot the pressure distribution along this center line in Fig. 18, where the shaded region depicts the area between the 10th and the 90th percentile of the published results in Berre et al. (2021) on similar meshes about $150k$ cells. It is observed from this figure that our results on both meshes are within the range of the published results in Berre et al. (2021), and that the results on the fitted mesh may be more accurate as it is closer to the reference solution from USTUTT-MPFA on a mesh with roughly 1 million cells.

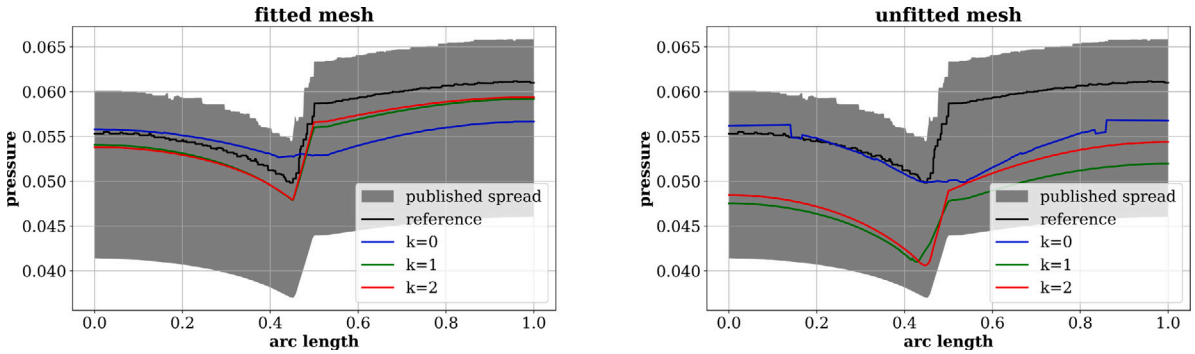

Fig. 18. Example 5. Pressure along line $(0.5, 1.1, 0) - -(0.5, 1.1, 1.0)$. Here reference data is the result from the USTUTT-MPFA scheme in Berre et al. (2021) on a mesh with roughly 1 million matrix elements. The shaded region depicts the area between the 10th and the 90th percentile of the published results in Berre et al. (2021) on similar meshes with about $150k$ cells.

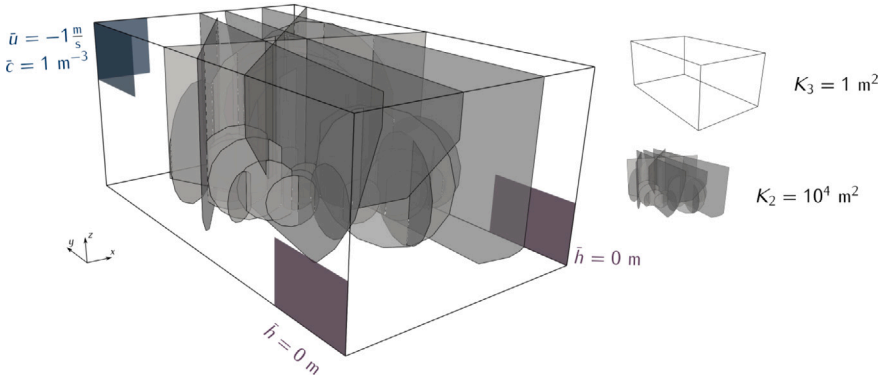

Fig. 19. Example 6. Conceptual model and geometrical description of the domain.

Table 2
Example 5. Choice of the penalty parameters for different polynomial degree and meshes.

k	Fitted mesh		Unfitted mesh	
	C_c	s_c	C_c	s_c
0	5	2	2.5	2
1	0.7	3	0.7	3
2	3.5	3	0.7	3

Example 6 (*Field Case in 3D*)**.** In our final numerical example, we consider a similar setting as the last benchmark case proposed in Berre et al. (2021). The geometry is based on a postprocessed outcrop from the island of Algerøyna, outside Bergen, Norway, which contains 52 fracture. The simulation domain is the box $\Omega = (-500, 350) \times (100, 1500) \times (-100, 500)$. The fracture geometry is depicted in Fig. 19. Homogeneous Dirichlet boundary condition is imposed on the outlet boundary

$$\partial\Omega_{out} := \underbrace{\{-500\} \times (100, 400) \times (-100, 100)}_{\partial\Omega_{out,0}} \cup \underbrace{\{350\} \times (100, 400) \times (-100, 100)}_{\partial\Omega_{out,1}}$$

uniform unit inflow $\boldsymbol{u} \cdot \boldsymbol{n} = 1$ is imposed on the inlet boundary

$$\partial\Omega_{in} := \underbrace{\{-500\} \times (1200, 1500) \times (300, 500)}_{\partial\Omega_{in,0}} \cup \underbrace{(-500, -200) \times \{1500\} \times (300, 500)}_{\partial\Omega_{in,1}}.$$

Matrix permeability is $\mathbb{K}_m = 1$, and fracture thickness is $\epsilon = 10^{-2}$. Similar to Example 3 in 2D, we consider three subcases: (a) all conductive fractures with permeability $k_c = 10^4$, (b) all blocking fractures with permeability $k_b = 10^{-4}$ m^2, and (c) 2 blocking fractures with $k_b = 10^{-4}$ and 50 conductive fractures with $k_c = 10^4$. Location of the blocking/conductive fractures for case (c) are marked in red/blue in the right panel of Fig. 20.

We perform the method (5) on two unfitted meshes; see Fig. 20 for the fine mesh. The coarse mesh contains $27k$ tetrahedral cells which is obtained by performing two steps of local mesh refinement around the fractured cells of a uniform background mesh with $h \approx 200$. And the fine mesh contains $210k$ cells with $57.6k$ fractured cells which spits to 47.8 conductive fractured cells and $9.8k$ blocking fractured cells for case (c), which is a further uniform refinement of that coarse mesh. As in the previous examples, we take polynomial degree $k = 0, 1, 2$. For the penalty parameters, we take $C_b = 1$, $s_b = 2$, $C_c = 1$ and the scaling power $s_c = 3$ for $k = 1$ and $k = 2$, and $s_c = 1$ for $k = 0$. Moreover, for the case $k = 0$ the default choice of stabilization (5h) is too strong which leads to almost constant (zero) pressure approximations for case (a). Here we further reduce the stabilization for $k = 0$ by a factor of $L = 1400$.

The pressure along the two diagonal lines $(-500, 100, -100)$–$(350, 1500, 500)$ and $(350, 100, -100)$–$(-500, 1500, 500)$ are shown in Figs. 21–23 for all three cases, where for case (a) the shaded region depicts the area between the 10th and the 90th percentile of the published results in Berre et al. (2021) on fitted meshes with about $260k$ cells. It is observed that all methods produce qualitatively similar results for each case, even on the coarse mesh. And our results for case (a) is consistent with the published results in Berre et al. (2021).

We now plot the pressure profile on the fine mesh for $k = 2$ for the three cases in Fig. 24. These contour plots are similar to the 2D results where the effects of conductive and blocking fractures are completely different as expected.

Let us finally briefly comment on the computational cost on the fine mesh where the major bottleneck is the global linear system solve. Here

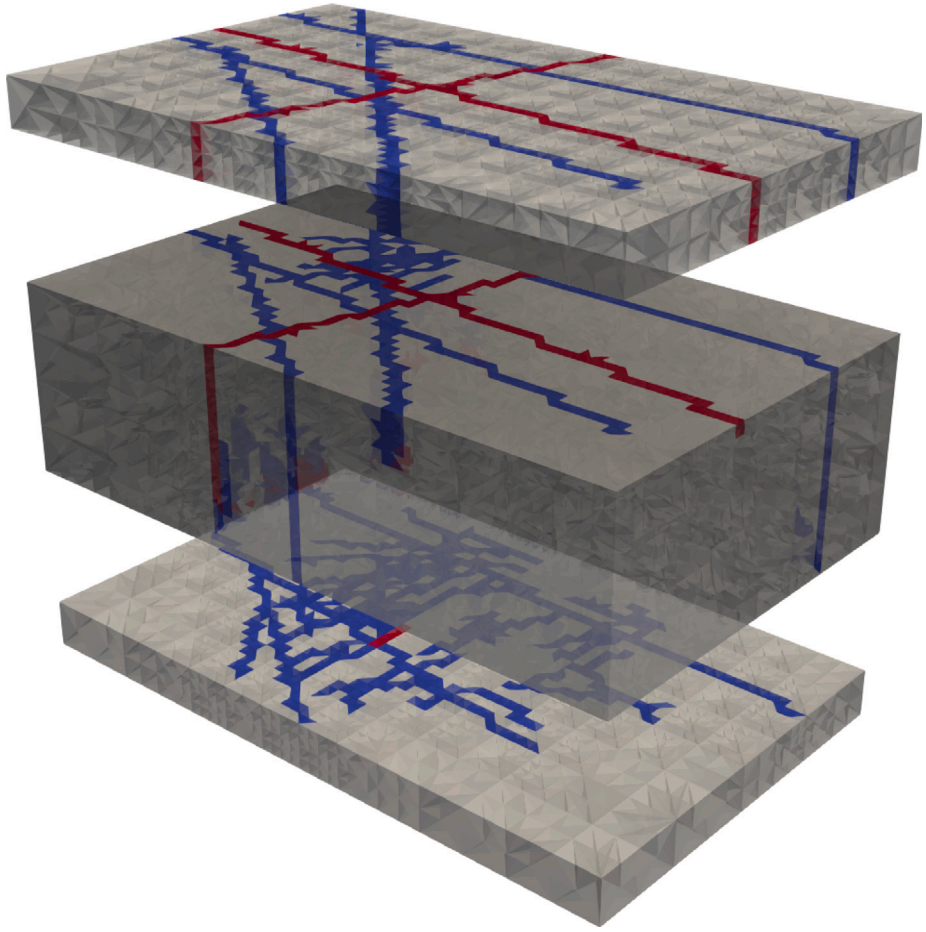

Fig. 20. Example 6. Blocking (red) and conductive (blue) fractured cells on the fine mesh with 216 816 cells for case (c). Here the mesh is translated in the z-direction for $z < 100$ and $z > 400$ for better data visualization.

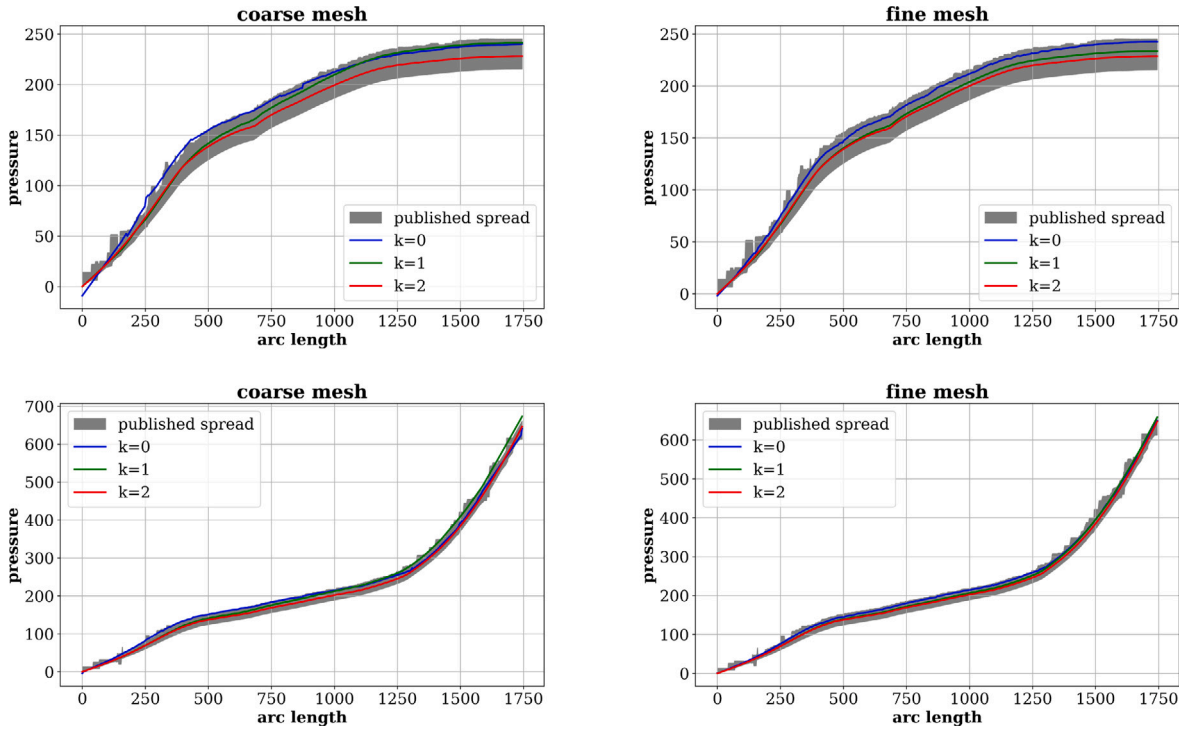

Fig. 21. Example 6: Case (a). Pressure along line $(-500, 100, -100)$–$(350, 1500, 500)$ (top) and line $(350, 100, -100)$–$(-500, 1500, 500)$ (bottom). The shaded region depicts the area between the 10th and the 90th percentile of the published results in Berre et al. (2021) on fitted meshes with about $260k$ cells.

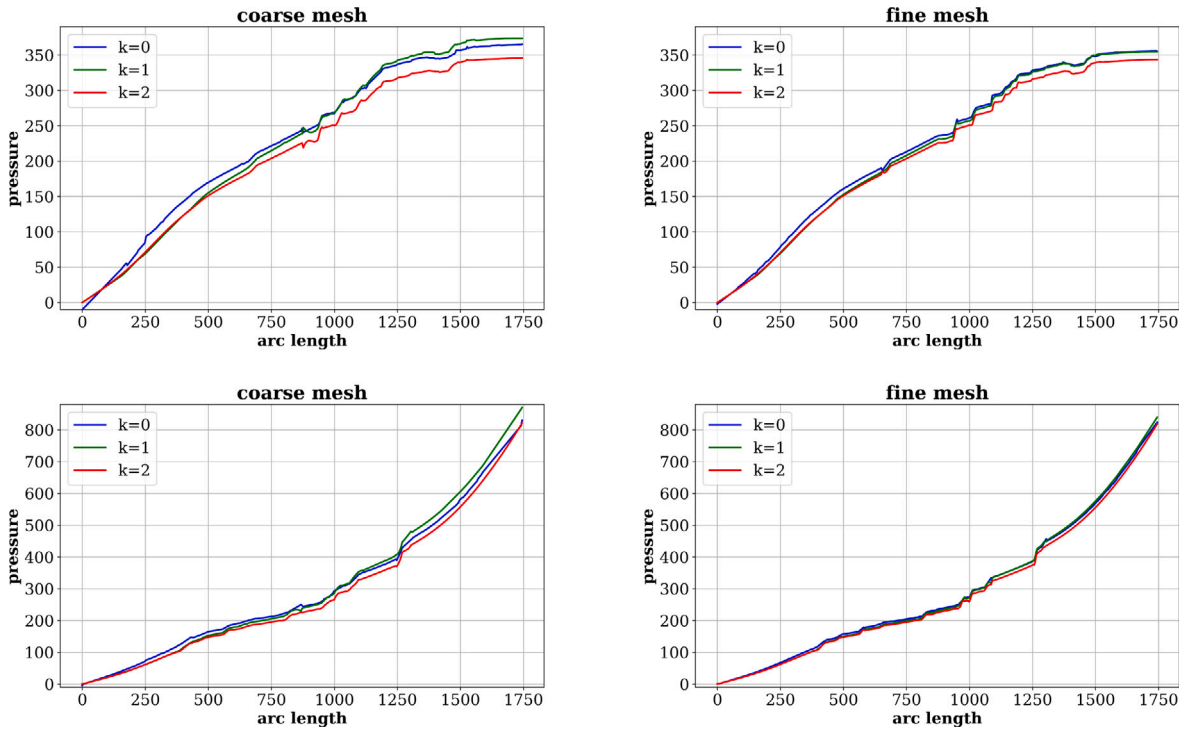

Fig. 22. Example 6: Case (b). Pressure along line $(-500, 100, -100)$–$(350, 1500, 500)$ (top) and line $(350, 100, -100)$–$(-500, 1500, 500)$ (bottom).

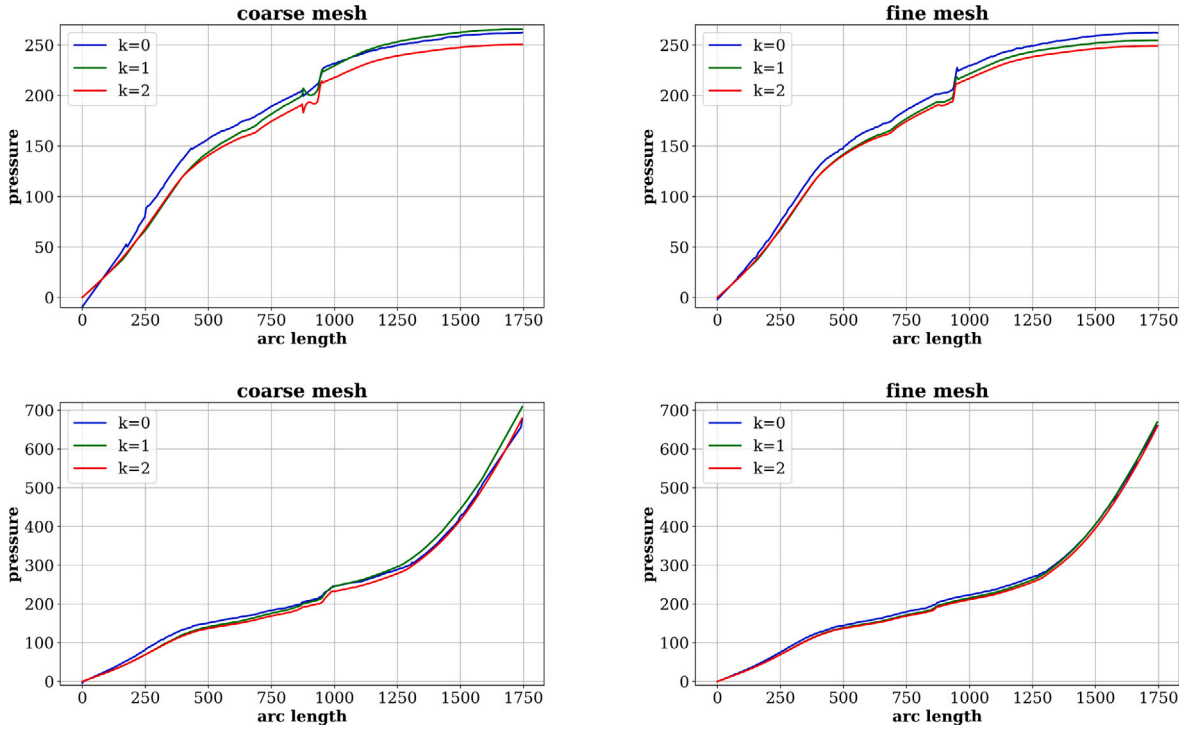

Fig. 23. Example 6: Case (c). Pressure along line $(-500, 100, -100)$–$(350, 1500, 500)$ (top) and line $(350, 100, -100)$–$(-500, 1500, 500)$ (bottom).

we use NGSolve's built-in parallel sparse Cholesky factorization to solve this global SPD linear system on a 64-core server with two AMD EPYC 7532 processors which has 256 G memory. For $k = 0$, there are $439k$ global DOFs, and the linear system solver takes 30 G memory and 4 s wall clock time; for $k = 1$, there are 1.32 million global DOFs, and the linear system solver takes 50 G memory and 48 s wall clock time; for $k = 2$, there are 2.64 million global DOFs, and the linear system solver takes 100 G memory and 285 s wall clock time. More efficient solver like multigrid may significantly reduce the memory consumption and overall solver time. We will investigate this issue in our future work.

4. Conclusion

We presented a novel HDG scheme on unfitted meshes for fractured porous media flow with both blocking and conductive fractures based on the RDFM using Dirac-δ functions approach to handle the fractures.

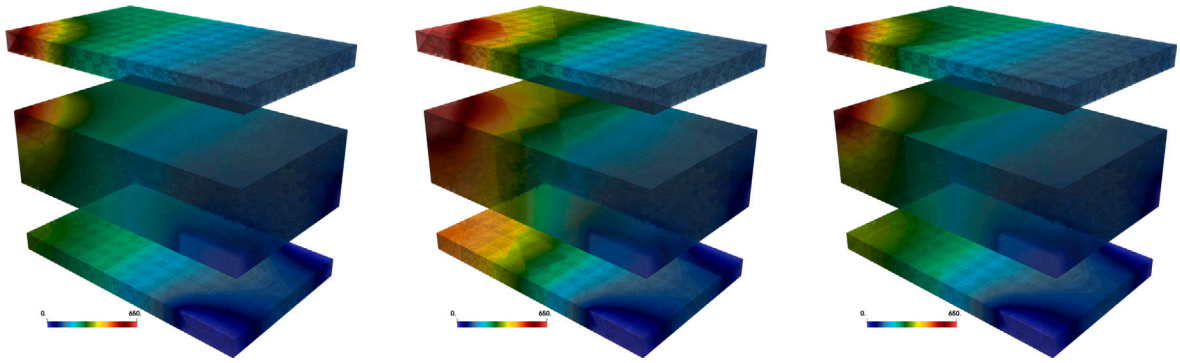

Fig. 24. Example 6. Pressure contour for $k = 2$ on the fine mesh. Left: case (a). Middle: case (b). Right: case (c).

Well-posedness of the method is established. Our scheme has a simple form, which can simultaneously handle blocking and conductive fractures using unfitted meshes. In fact, we simply modify a regular porous media flow HDG solver by including two surface integrals related to the blocking and conductive fractures which are represented as (multi-)level set functions, and properly adjust the penalty parameters in the numerical flux on those fractured cells. No lower dimensional fracture modeling is needed in our approach. Besides the ease of using unfitted meshes in our scheme, we also maintain local conservation as typical of DG methodologies. Moreover, the resulting linear system can be solved efficiently via static condensation, which leads to a global coupled SPD linear system, and higher order pressure postprocessing is also available. The proposed HDG scheme is extensively tested against various benchmark examples in two- and three-dimensions. Satisfactory results are observed even when both blocking and conductive fractures co-exist in the computational domain.

Our future work includes the detailed study of the stabilization function on the performance of the scheme, and their variable-order and hybrid-mixed variants. We will also investigate robust preconditioning techniques for the global SPD linear system, and extend our solver to multiphase fractured porous media flows.

CRediT authorship contribution statement

Guosheng Fu: Methodology, Writing – original draft, Software, Investigation, Funding acquisition. **Yang Yang:** Conceptualization, Methodology, Writing – review & editing, Funding acquisition.

Declaration of competing interest

The authors declare that they have no known competing financial interests or personal relationships that could have appeared to influence the work reported in this paper.

Data availability

Code has been give in the manuscript

References

Alboin, C., Jaffré, J., Roberts, J., Serres, C., 1999. Domain decomposition for flow in porous media with fractures. In: Lai, M.C.C.H., Bjorstad, P.E., Widlund, O. (Eds.), Domain Decomposition Methods in Sciences and Engineering, Vol. 53. Domain Decomposition Press, Bergen, Norway, pp. 365–373.

Alboin, C., Jaffré, J., Roberts, J.E., Wang, X., Serres, C., 2000. Domain decomposition for some transmission problems in flow in porous media. In: Numerical Treatment of Multiphase Flows in Porous Media. Springer, Heidelberg, Berlin, pp. 22–34.

Angot, P., Boyer, F., Hubert, F., 2009. Asymptotic and numerical modelling of flows in fractured porous media. ESAIM Math. Model. Numer. Anal. 43 (2), 239–275.

Baca, R.G., Arnett, R.C., Langford, D.W., 1984. Modelling fluid flow in fractured-porous rock masses by finite-element techniques. Internat. J. Numer. Methods Fluids 4 (4), 337–348.

Barenblatt, G.I., Zheltov, I.P., Kochina, I.N., 1960. Basic concepts in the theory of seepage of homogeneous liquids in fissured rocks [strata]. J. Appl. Math. Mech. 24 (5), 1286–1303.

Berre, I., Boon, W., Flemisch, B., Fumagalli, A., Gläser, D., Keilegavlen, E., Scotti, A., Stefansson, I., Tatomir, A., Brenner, K., Burbulla, S., Devloo, P., Duran, O., Favino, M., Hennicker, J., Lee, I.-H., Lipnikov, K., Masson, R., Mosthaf, K., Nestola, M.C., Ni, C.-F., Nikitin, K., Schädle, P., Svyatskiy, D., Yanbarisov, R., Zulian, P., 2021. Verification benchmarks for single-phase flow in three-dimensional fractured porous media. Adv. Water Resour. 147, 103759.

Boon, W., Nordbotten, J., Yotov, I., 2018. Robust discretization of flow in fractured porous media. SIAM J. Numer. Anal. 56, 2203–2233.

Burman, E., Hansbo, P., Larson, M.G., Larsson, K., 2019. Cut finite elements for convection in fractured domains. Comput. & Fluids 179, 726–734.

Cockburn, B., Dubois, O., Gopalakrishnan, J., Tan, S., 2014. Multigrid for an HDG method. IMA J. Numer. Anal. 34 (4), 1386–1425.

Cockburn, B., Gopalakrishnan, J., Lazarov, R., 2009. Unified hybridization of discontinuous Galerkin, mixed and continuous Galerkin methods for second order elliptic problems. SIAM J. Numer. Anal. 47, 1319–1365.

Cockburn, B., Gopalakrishnan, J., Sayas, F.-J., 2010. A projection-based error analysis of HDG methods. Math. Comp. 79, 1351–1367.

Feng, W., Guo, H., Xu, Z., Yang, Y., 2021. Conservative numerical methods for the reinterpreted discrete fracture model on non-conforming meshes and their applications in contaminant transportation in fractured porous media. Adv. Water Resour. 153, 103951(16).

Flemisch, B., Berre, I., Boon, W., Fumagalli, A., Schwenck, N., Scotti, A., Stefansson, I., Tatomir, A., 2018. Benchmarks for single-phase flow in fractured porous media. Adv. Water Resour. 111, 239–258.

Flemisch, B., Fumagalli, A., Scotti, A., 2016. A review of the XFEM-based approximation of flow in fractured porous media. In: Advances in Discretization Methods. Springer, Cham, pp. 47–76.

Fu, G., 2021. Uniform auxiliary space preconditioning for HDG methods for elliptic operators with a parameter dependent low order term. SIAM J. Sci. Comput. 43 (6), A3912–A3937.

Fu, G., Yang, Y., 2022. A hybrid-mixed finite element method for single-phase Darcy flow in fractured porous media. Adv. Water Resour. 161, 104129.

Fumagalli, A., Scotti, A., 2014. An efficient XFEM approximation of Darcy flows in arbitrarily fractured porous media. Oil Gas Sci. Technol.–Rev. d'IFP Energies Nouvelles 69 (4), 555–564.

Geiger, S., Dentz, M., Neuweiler, A.I., 2013. Novel multi-rate dual-porosity model for improved simulation of fractured and multiporosity reservoirs. SPE J. 4, 670–684.

Geiger-Boschung, S., Matth"ai, S.K., Niessner, J., Helmig, R., 2009. Black-oil simulations for three-component, three-phase flow in fractured porous media. SPE J. 14 (02), 338–354.

Ghorayeb, K., Firoozabadi, A., 2000. Numerical study of natural convection and diffusion in fractured porous media. SPE J. 5, 12–20.

Hansbo, A., Hansbo, P., 2002. An unfitted finite element method, based on nitsche's method, for elliptic interface problems. Comput. Methods Appl. Mech. Engrg. 191 (47–48), 5537–5552.

HosseiniMehr, M., Cusini, M., Vuik, C., Hajibeygi, H., 2018. Algebraic dynamic multilevel method for embedded discrete fracture model (F-ADM). J. Comput. Phys. 373, 324–345.

HosseiniMehr, M., Tomala, J.P., Vuik, C., Kobaisi, M.A., Hajibeygi, H., 2022. Projection-based embedded discrete fracture model (pEDFM) for flow and heat transfer in real-field geological formations with hexahedral corner-point grids. Adv. Water Resour. 159, 104091.

Huang, H., Long, T.A., Wan, J., Brown, W.P., 2011. On the use of enriched finite element method to model subsurface features in porous media flow problems. Comput. Geosci. 15 (4), 721–736.

Jiang, J., Younis, R.M., 2017. An improved projection-based embedded discrete fracture model (pEDFM) for multiphase flow in fractured reservoirs. Adv. Water Resour. 109, 267–289.

Kadeethum, T., Nick, H., Lee, S., Ballarin, F., 2020. Flow in porous media with low dimensional fractures by employing enriched Galerkin method. Adv. Water Resour. 142, 103620.

Karimi-Fard, M., Firoozabadi, A., 2001. Numerical simulation of water injection in 2D fractured media using discrete-fracture model. In: SPE annual technical conference and exhibition. Society of Petroleum Engineers.

Kim, J.G., Deo, M.D., 1999. Comparison of the performance of a discrete fracture multiphase model with those using conventional methods. In: SPE Reservoir Simulation Symposium. Society of Petroleum Engineers.

Kim, J.G., Deo, M.D., 2000. Finite element, discrete-fracture model for multiphase flow in porous media. AIChE J. 46 (6), 1120–1130.

Köppel, M., Martin, V., Jaffré, J., Roberts, J.E., 2019a. A Lagrange multiplier method for a discrete fracture model for flow in porous media. Comput. Geosci. 23 (2), 239–253.

Köppel, M., Martin, V., Roberts, J.E., 2019b. A stabilized Lagrange multiplier finite-element method for flow in porous media with fractures. GEM-Int. J. Geomath. 10, 7, (2019).

Lehrenfeld, C., Heimann, F., Preuß, J., von Wahl, H., 2021. `ngsxfem`: Add-on to ngsolve for geometrically unfitted finite element discretizations. J. Open Source Softw. 6 (64), 3237.

Li, L., Lee, S.H., 2008. Efficient field-scale simulation of black oil in a naturally fractured reservoir through discrete fracture networks and homogenized media. SPE Reserv. Eval. Eng. 11 (04), 750–758.

Martin, V., Jaffré, J., Roberts, J.E., 2005. Modeling fractures and barriers as interfaces for flow in porous media. SIAM J. Sci. Comput. 26 (5), 1667–1691.

Moinfar, A., 2013. Development of an Efficient Embedded Discrete Fracture Model for 3D Compositional Reservoir Simulation in Fractured Reservoirs (Ph.D. Thesis). University of Texas, Austin.

Noorishad, J., Mehran, M., 1982. An upstream finite element method for solution of transient transport equation in fractured porous media. Water Resour. Res. 18 (3), 588–596.

Odsæter, L.H., Kvamsdal, T., Larson, M.G., 2019. A simple embedded discrete fracture–matrix model for a coupled flow and transport problem in porous media. Comput. Methods Appl. Mech. Engrg. 343, 572–601.

Salimzadeh, S., Khalili, N., 2015. Fully coupled XFEM model for flow and deformation in fractured porous media with explicit fracture flow. Int. J. Geomech. 16 (4), 04015091.

Schädle, P., Zulian, P., Vogler, D., Bhopalam, S.R., Nestola, M.G., Ebigbo, A., Krause, R., Saar, M.O., 2019. 3D non-conforming mesh model for flow in fractured porous media using Lagrange multipliers. Comput. Geosci. 132, 42–55.

Schöberl, J., 2014. C++11 Implementation of Finite Elements in NGSolve. ASC Report 30/2014, Institute for Analysis and Scientific Computing, Vienna University of Technology.

Schwenck, N., 2015. An XFEM-Based Model for Fluid Flow in Fractured Porous Media (Ph.D. Thesis). Universität Stuttgart.

Tene, M., Bosma, S., Al Kobaisi, M., Hajibeygi, H., 2017. Projection-based embedded discrete fracture model (pEDFM). Adv. Water Resour. 105, 205–216.

Warren, J.E., Root, P.J., 1963. The behavior of naturally fractured reservoirs. Soc. Pet. Eng. J. 3, 245–255.

Xu, Z., Huang, Z., Yang, Y., 2023. The hybrid-dimensional Darcy's law: a non-conforming reinterpreted discrete fracture model (RDFM) for single-phase flow in fractured media. J. Comput. Phys. 473, 111749.

Xu, J., Sun, B., Chen, B., 2019. A hybrid embedded discrete fracture model for simulating tight porous media with complex fracture systems. J. Pet. Sci. Eng. 174, 131–143.

Xu, Z., Yang, Y., 2020. The hybrid dimensional representation of permeability tensor: A reinterpretation of the discrete fracture model and its extension on nonconforming meshes. J. Comput. Phys. 415, 109523.

Yan, X., Huang, Z., Yao, J., Li, Y., Fan, D., 2016. An efficient embedded discrete fracture model based on mimetic finite difference method. J. Pet. Sci. Eng. 145, 11–21.

Zhang, N., Yao, J., Huang, Z., Wang, Y., 2013. Accurate multiscale finite element method for numerical simulation of two-phase flow in fractured media using discrete-fracture model. J. Comput. Phys. 242, 420–438.